

STANDARDIZED MEASUREMENTS OF THE LIGHT-TO-HEAT OUTPUT OF
STRUCTURALLY-COMPLEX METALLIC NANOPARTICLES USED IN PHOTOTHERMAL
THERAPIES

A Thesis

by

NAMRATHA RAJKUMAR BHAT

Submitted to the Office of Graduate and Professional Studies of
Texas A&M University
in partial fulfillment of the requirements for the degree of
MASTER OF SCIENCE

Chair of Committee,	Samuel Mabbott
Committee Members,	Gerard L. Coté Ya Wang
Head of Department,	Mike McShane

December 2020

Major Subject: Biomedical Engineering

Copyright 2020 Namratha Rajkumar Bhat

ABSTRACT

Photothermal therapy is a type of treatment method that uses the thermal properties of light to destroy tumors inside the body. It employs photothermal agents, such as nanoparticles that efficiently convert the incoming light into heat. When these nanoparticles are placed inside tumor cells, the heat generated changes the physiology and ultimately destroys the tumor cells. For this application, many different shapes, sizes and materials of nanoparticles are being explored by researchers. However, there are currently no standardized, easy-to-use methods for prescreening the heat output from generated by these nanoparticles before performing in-vivo and in-vitro tests. To solve this issue, we worked on developing a user-friendly pre-screening approach that can be used to measure the heat output generated by different nanoparticles prior to using animal models. Our system incurred several iterative changes in order to improve the reproducibility of heat measurements. We tested out our system using 2 types of gold nanoparticles: nanostars and nanoprisms. We performed different experiments to study the heating properties and morphological changes of these nanoparticles during the course of heating to understand their viability as photothermal agents. Both nanoparticles effectively converted light to heat but both sets of particles were susceptible to aggregation. We also measured the ability of each particle type to enhance the Raman spectra of two common thiol-containing Raman reporters; 4- mercaptobenzoic acid and benzene-1,4-dithiol whilst also converting light-to-heat.

DEDICATION

To my mother, my father and sister.

ACKNOWLEDGMENTS

I would like to thank my research advisor and committee chair, Dr. Mabbott for the countless hours of professional advising and helping me achieve my research goals. I learned many lessons from him including how to conduct research in a meticulous & ordered fashion and how to better present my work to the scientific community. I would also like to thank the rest of my committee (Dr. Coté and Dr. Wang) for their guidance and support throughout the course of this project. I would also like to thank Suhas Chavva for guiding me along the way and answering all my endless questions.

I also want to thank my colleagues, the department faculty and my lab mates (Angela San Juan, Siddhant Jaitpal and John Dean) for helping me and making my time in graduate school a great experience.

Finally, thank you to my family for all of the love and support they gave me throughout my 2 years in College Station. My mother and father who have been my pillars throughout this journey. I would also like to thank my sister, Sneha, for always making me laugh and livening my spirits during hard times.

CONTRIBUTORS AND FUNDING SOURCES

Contributors

This thesis committee for this work include Dr.Mabbott (Chair) from the Department of Biomedical Engineering, Dr.Coté from the Department of Biomedical Engineering and Dr.Wang from the Department of Mechanical Engineering at Texas A&M University .

Funding Sources

The research was supported by Dr. Mabbott's TEES and departmental start-up funds.

NOMENCLATURE

NP	Nanoparticles
PTT	Photothermal Therapy
NIR	Near Infra-red
PT	Photothermal
SPR	Surface Plasmon Resonance
UV-vis	Ultraviolet-Visible
ctab	cetyltrimethylammonium bromide
SERS	Surface Enhanced Raman Spectroscopy
DI	De-Ionized
NS	Nanostars
NPrs	Nanoprisms
TEM	Transmission Electron Microscope
ABS	Acrylonitrile butadiene styrene
pla	Polylactic Acid
4-mba	4-Mercaptobenzoic acid
bdt	Benzene-1,4-dithiol
peg	Polyethylene glycol

TABLE OF CONTENTS

	Page
ABSTRACT	ii
DEDICATION	iii
ACKNOWLEDGMENTS	iv
CONTRIBUTORS AND FUNDING SOURCES	v
NOMENCLATURE	vi
TABLE OF CONTENTS	vii
LIST OF FIGURES	ix
LIST OF TABLES.....	xiii
1. INTRODUCTION.....	1
1.1 Background.....	1
1.2 PTT	1
1.3 Electron Processes when a metallic NP is exposed to Light	2
1.4 Metal NPs	3
1.5 NIR Region.....	5
1.6 Imaging NPs inside the body	5
1.6.1 SERS	6
1.7 Photothermal Standardization	6
1.8 Current Approaches Measuring Photothermal Output: In-Solution, In-Vitro and In-Vivo	7
2. MATERIALS AND METHODS	12
2.1 Materials.....	12
2.2 NP Synthesis	12
2.2.1 Gold nanosphere (seed) synthesis	12
2.2.2 Gold nanostar (AuNS) synthesis	13
2.2.3 Gold Nanoprism (AuNPr) Synthesis	13
2.3 Characterization Techniques.....	14
2.4 Heating Setup for prescreening.....	14
2.5 Temperature measurement device	15
2.6 Temperature data processing	16

2.7	1064 nm laser system	17
2.8	785 nm laser system.....	17
2.9	Heating Experiments	19
2.9.1	Stability of NPs	19
2.9.2	Effect of Citrate buffer on NS solution	19
2.9.3	Effect of volume on heat output	20
2.9.4	Change in NP morphology: before and after heating	20
2.9.5	NP exposure to multiple heat/cool cycles	21
2.10	SERS Enhancement	21
2.10.1	SERS Enhancement Procedure	22
3.	RESULTS.....	23
3.1	Temperature Measurement Device	23
3.2	Characterization of Gold nanospheres	24
3.3	Characterization of Gold nanostar (AuNS)	25
3.4	Characterization of Gold Nanoprism	26
3.5	Cuvette Based Heating Setup.....	29
3.6	AuNS	29
3.6.1	Overnight storage of NPs and effects on shape and UV-vis-NIR spectra.....	29
3.6.2	Effect of Citrate Buffer on stability of AuNS	32
3.6.3	Effect of volume of sample	34
3.6.3.1	785 nm System	34
3.6.3.2	1064 nm System.....	35
3.6.4	Change in morphology before and after heating	36
3.6.5	Exposure to multiple heat and cool cycles	38
3.7	AuNPr	39
3.7.1	Overnight storage of NPs and effects on shape and UV-vis-NIR spectra.....	39
3.7.2	Effect of volume of sample	40
3.7.2.1	785 nm System	40
3.7.2.2	1064 nm system	41
3.7.3	Change in morphology before and after heating	42
3.7.4	Exposure to multiple heat and cool cycles	44
3.8	SERS Enhancement	45
3.8.1	MBA	45
3.8.2	BDT.....	51
4.	SUMMARY AND CONCLUSIONS	56
4.1	Future Work	57
	REFERENCES	58
	APPENDIX A. ARDUINO MICROCONTROLLER CODE	65

LIST OF FIGURES

FIGURE	Page
1.1 Schematic representation of various processes activated when a light beam interacts with a NP. The presence of scattering, absorption and heat generation are included. Heat occurs as a result of light absorption	2
1.2 Schematic illustration of the physiological and biological effects of gold NP-mediated PTT. A large amount of gold NP accumulates due to the leaky vasculature of the tumor, resulting in a PT effect in response to NIR light ultimately inducing apoptosis and necrosis of tumor tissue	3
1.3 Schematic illustration of different electron processes that occur when a gold NP is illuminated with light	4
1.4 Schematic illustration of different electron processes that occur when an Au NP is illuminated with light	4
1.5 Spectrum of light demonstrating the biological optical window in the NIR region. Image shows maximum penetration of light at 750 nm up to 5 mm .Reprinted from "Opportunities and challenges of fluorescent carbon dots in translational optical imaging" [20]	6
1.6 Spectrum of light demonstrating the absorption coefficients of 4 different biological components in the NIR region with NIR Window 1 and 2 (aka Short Wave Infrared Window). Reprinted from "Review of biomedical applications of contactless imaging of neonates using infrared thermography and beyond" [21].....	7
1.7 Image represents setup used by Govorov et al, wherein NPs are embedded in ice in a glass chamber. A thermocouple is also embedded to record temperature changes. A focused laser beam is used to heat the NPs. Reprinted from "Generating heat with metal nanoparticles"[27]	9
2.1 AuNS Synthesis protocol developed from the seed mediated procedure yielding a blue-green mixture of NSs with an absorbance at 820 nm	14
2.2 AuNPr Synthesis protocol yielding a brown mixture of NPr with an absorbance at 1000 nm	15

2.3	Image of the initial 1064 nm laser system screwed onto an optical table. Focusing lens placed at an optimal distance allowing a sharp laser spot in the middle of the cuvette. Temperature sensor inserted into the cuvette from the top to measure sample temperature.	17
2.4	View of the 785 nm laser system designed to measure heat output from the sample in the cuvette using a thermocouple. Black anodised box present behind the cuvette and prevent background noise for SERS Enhancement	18
3.1	Testing results for sensor 1,2 ,3 and 4 (data provided in Table 2.1) samples were heated at a rate of 0.865°C/min. Data comp for 30 mins. Thermocouple measured samples were compared with a calibrated mercury thermometer (Orange)	24
3.2	Au nanosphere Characterization with a λ_{max} of 519 nm with an absorbance of 0.88. The TEM image of the NP seed shows NPs with 30 ± 5 nm diameters. Sample is wine red in color	25
3.3	Au nanostar Characterization with a λ_{max} of 820 nm with an absorbance of 0.38. The TEM image of the NS shows 75 nm Au cores with 15 nm arms. Sample is light blue in color	26
3.4	UV-vis NIR Spectra of NPrs displaying 2 peaks where one corresponded to the length of the AuNPr while the other corresponded to the height of the prism	27
3.5	Au nanoprism characterization from method1 by Beatriz showing 2 peaks at 535 nm and 950 nm. The TEM image of the AuNPrs showed a heterogeneous mixture of both spherical and triangular shaped particles.Triangular particles had lengths ranging from 40 to 90 nm, while spherical particles had a diameter of 5-30 nm. Sample is dark brown in color	28
3.6	Au nanoprism characterization from method2 by Gabriel showing 2 peaks at 535 nm and 1000 nm. The TEM image of the AuNPrs showed a heterogeneous mixture of both spherical and triangular shaped particles.Triangular particles had lengths ranging from 30 to 80 nm, while spherical particles had a diameter of 5-30 nm. Sample is dark brown in color	29
3.7	The figure shows the Vis-NIR-Spectra comparison of the AuNS on the first day of creation (Blue curve) and blueshift of the spectra on the second day (Orange curve) .	30
3.8	The graph alongside demonstrates the heating profile difference between the same sample heated on 2 consecutive days	31
3.9	TEM Characterization of NS (A) Day1 before heating, (B) Day2 before heating, (C) Day1-After heating, (D) Day2-After heating.....	32
3.10	The graph demonstrates blueshift of NSs over a course of 1 week when they were not capped with a citrate buffer	33

3.11	The graph demonstrates blueshift of NSs over a course of 1 week when they were capped with a citrate buffer	34
3.12	Heating data comparison of samples of AuNSs with differing volumes (300 μL , 200 μL and 100 μL) heated using the 785 nm laser system	35
3.13	Heating data comparison of samples of AuNSs with differing volumes (300 μL , 200 μL and 100 μL) heated using the 1064 nm laser system	36
3.14	TEM image of NSs before and after being exposed to the laser light	37
3.15	Normalized UV-vis-NIR Spectra of AuNS before and after being exposed to the NIR laser.....	37
3.16	The figures demonstrate AuNS heated for 20-minute heat-15-minute cool cycles with the 785 nm laser system.....	38
3.17	The figure shows the Absorption Spectra comparison of the AuNPr on the first day of creation (Blue curve) and the spectra on the second day (Orange curve)	39
3.18	Heating profile of nanoprisms taken on 2 consecutive days after overnight storage at 4 $^{\circ}\text{C}$	40
3.19	Heating data comparison of samples of AuNPrs with differing volumes (300 μL , 200 μL and 100 μL) heated using the 785 nm laser system	41
3.20	Heating data comparison of samples of AuNPr with differing volumes (300 μL , 200 μL and 100 μL) heated using the 1064 nm laser system	42
3.21	TEM image of NPr before and after being exposed to the laser light	43
3.22	Normalized UV-vis-NIR Spectra of AuNPr before and after being exposed to the NIR Laser	43
3.23	The figure demonstrates AuNPr heated for 20-minute heat-15-minute cool cycles with the 785 nm laser system.....	44
3.24	Complete SERS spectrum of MBA AuNS taken during a 20 min heating cycle	45
3.25	Comparison of SERS intensity change of MBA AuNS at 1081 cm^{-1} during 20-minute heating cycle	46
3.26	Comparison of SERS intensity change of MBA AuNS at 1591 cm^{-1} using 20-minute heating cycle	47
3.27	Comparison between SERS intensity change of MBA AuNS with temperature change of the sample during the 20-min heating cycle for peak1 (1081 cm^{-1}) and peak2 (1591 cm^{-1}).....	48

3.28	Complete SERS spectrum of MBA AuNPr taken during a 20 min heating cycle.	49
3.29	Comparison of SERS intensity change of MBA AuNPr at 1081 cm ⁻¹ during 20-minute heating cycle	49
3.30	Comparison of SERS intensity change of MBA AuNPr at 1571 cm ⁻¹ during 20-minute heating cycle	50
3.31	Comparison between SERS intensity change of MBA AuNPr with temperature change of the sample during the 20-minute heating cycle for peak1 (1081 cm ⁻¹) and peak2 (1571 cm ⁻¹)	51
3.32	Complete SERS spectrum of BDT AuNS taken during a 20 min heating cycle.	52
3.33	Comparison of SERS intensity change of BDT AuNS with a relatively flat enhancement during 20-minute heating cycle	52
3.34	Comparison of SERS intensity change of BDT AuNS at 1571 cm ⁻¹ during 20-minute heating cycle	53
3.35	Complete SERS spectrum of BDT AuNPr taken during a 20 min heating cycle	54
3.36	Comparison of SERS intensity change of BDT AuNPr with λ_{max} at 1078 cm ⁻¹ during 20-min heating cycle	54
3.37	Comparison of SERS intensity change of BDT AuNPr with λ_{max} at 1571 cm ⁻¹ during 20-min heating cycle	55

LIST OF TABLES

TABLE	Page
2.1 Comparison of 4 different sensors tested for accuracy	16
3.1 Chemical structure and Peak assignments of 4-MBA and 1,4 BDT	45

1. INTRODUCTION

1.1 Background

In 2020, cancer was the 2nd most common cause of death in the United States.[1] Owing to the nature of the disease and large spread of the tumor cells throughout the body, there is currently no fully comprehensive method to treat it.[2] Common approaches used by clinicians are: chemotherapy, radiotherapy or surgery. All 3 approaches have the potential to cause harm to healthy tissue and elicit a number of side-effects. Furthermore, they may also compromise the body's immune response, leading to increased risk of secondary cancers. In the pursuit of more targeted treatment methods, hyperthermia or thermal ablation have been explored. Both methods employ a localized increase in environmental temperature causing the destruction of tumor cells.[3] Initial thermal ablation approaches involved a heated probe or needle that was inserted into the tumor cell to cause a change in temperature but more recently researchers are looking at less invasive methods to achieve localized heating.[4]

One way of delivering targeted heat is by using metallic nanoparticles (NPs) which are efficient at converting light-to-heat(Figure 1.1). By applying heat in tumor specific locations, it is believed that NPs will considerably increase the clinical application of thermal therapies and reduce morbidity and inefficiencies due to off-target heating.[5] This therapy has been named Photothermal Therapy (PTT).

1.2 PTT

PTT is a minimally invasive, local treatment method that uses optically-active agents such as noble metal NPs (e.g., gold) to absorb electromagnetic energy to treat medical conditions.[6] In PTT, usually a near-infrared (NIR) laser is employed to destroy target tumor cells within a localized region. The energy from the light is converted into heat through optical absorption by photothermal (PT) absorbers. Over time, this process causes either partial or complete ablation of the disease site. Using selective PT absorbers aligned with optimized light sources, tumors can be targeted

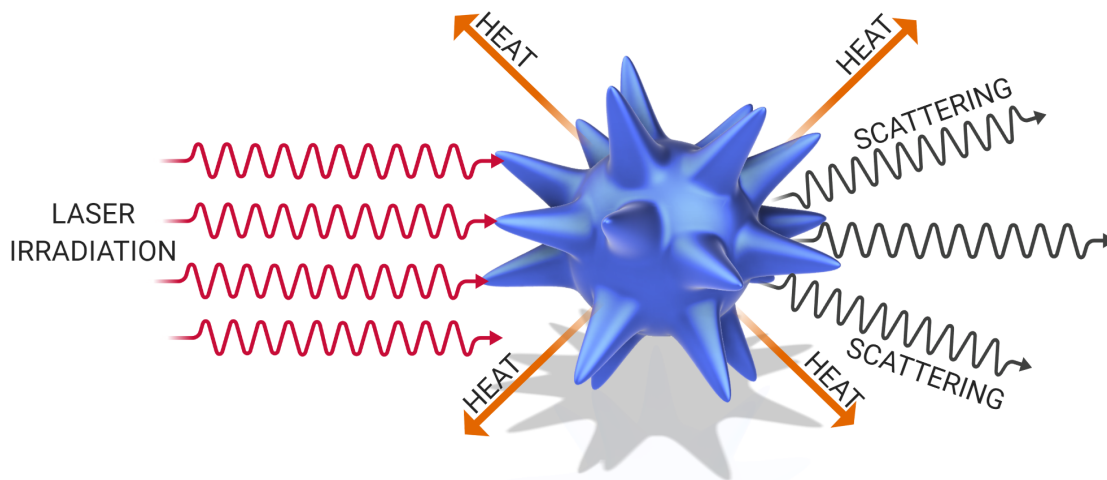


Figure 1.1: Schematic representation of various processes activated when a light beam interacts with a NP. The presence of scattering, absorption and heat generation are included. Heat occurs as a result of light absorption

with minimal invasiveness. This process which induces heat generation locally is already being employed as a treatment to kill cancer cells (Figure 1.2)[7]

PT conversion carried out using NPs is of huge interest to the biomedical field, with many researchers and academics believing that the use of these unique class of particles could signify a new era for modern medicine.[8] NPs can now be designed to have specific optical, physicochemical, biological, and pharmaceutical properties to enhance the strengths of PT cancer therapy and compensate for some of their toxicity.[9]

1.3 Electron Processes when a metallic NP is exposed to Light

When metallic NPs are exposed to light radiations, the free electrons in the metal transition from their ground state to excited state (Figure 1.3). They then undergo a non-radioactive decay and release heat to the local environment as they once again reach their ground state.[10] The oscillating electromagnetic field of the light induces a collective oscillation of the free electrons in the metal. These electron oscillations around the particle surface cause charge separation with respect to the ionic lattice, instigating the oscillation of dipoles along the direction of the lights electric field. The amplitude of the oscillation reaches its maximum at a specific frequency called



- 1 Nanoparticles accumulating in tumor sites due to leaky vasculature.
- 2 Heating of nanoparticles by near infrared light illumination and release of heat into surrounding medium.
- 3 Destruction of tumor cells as a result of change in temperature of the surrounding medium.

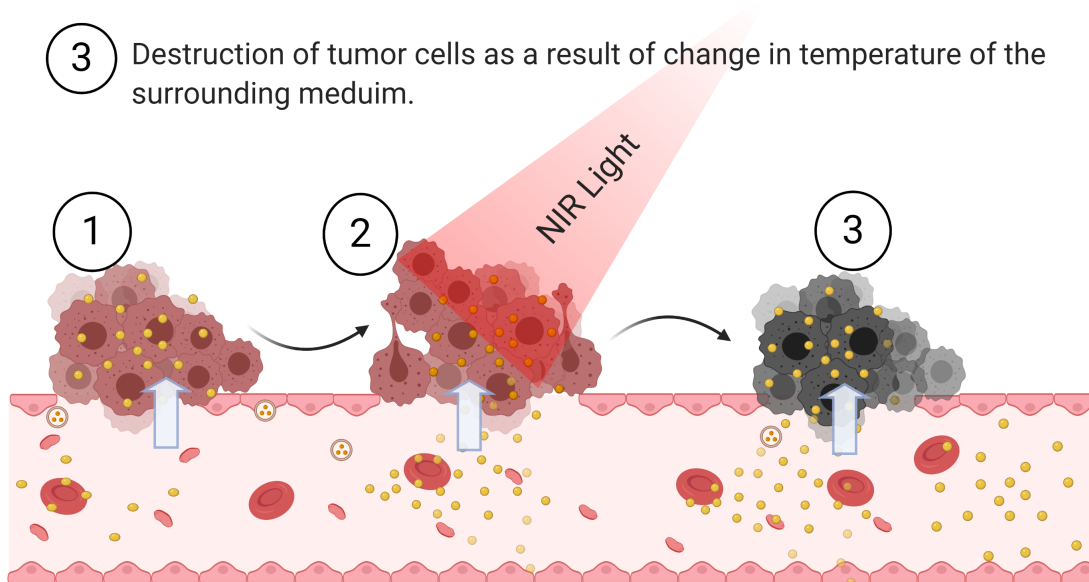


Figure 1.2: Schematic illustration of the physiological and biological effects of gold NP-mediated PTT. A large amount of gold NP accumulates due to the leaky vasculature of the tumor, resulting in a PT effect in response to NIR light ultimately inducing apoptosis and necrosis of tumor tissue

surface plasmon resonance (SPR) frequency (Figure 1.4). The SPR induces a strong absorption of the incident light and can be measured using a UV–vis spectrophotometer. The SPR band is much stronger for plasmonic (noble metal) NPs as compared to other metallic NPs.[11]

1.4 Metal NPs

In recent years, there has been tremendous development in nanotechnology leading to the exploration of various types and sizes of NPs with unique properties. Specific to cancer therapy and theranostics, metal NPs have been widely studied due to their remarkable optical properties and excellent absorption. Strong absorption is a pre-requisite for effective laser therapy at low laser

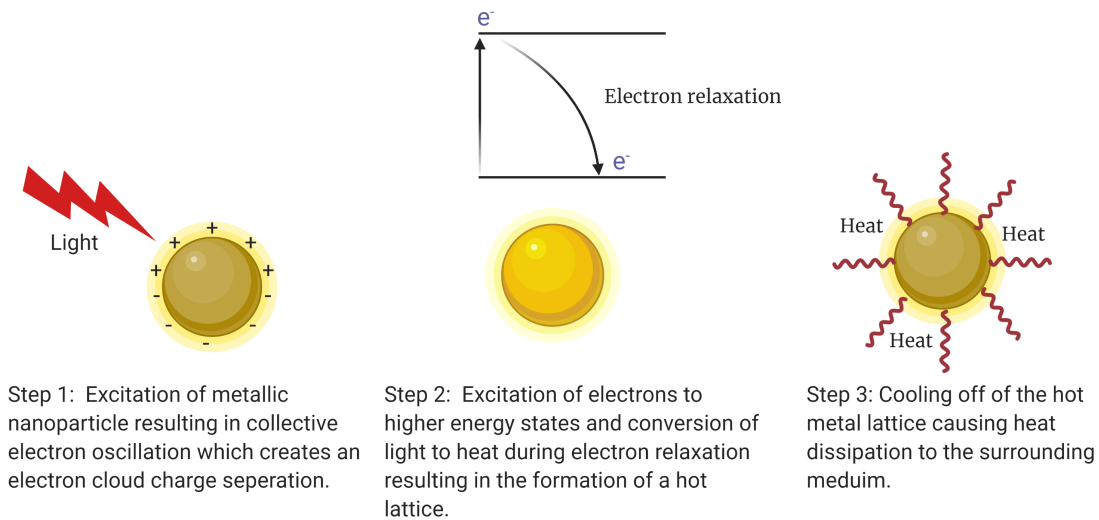


Figure 1.3: Schematic illustration of different electron processes that occur when a gold NP is illuminated with light

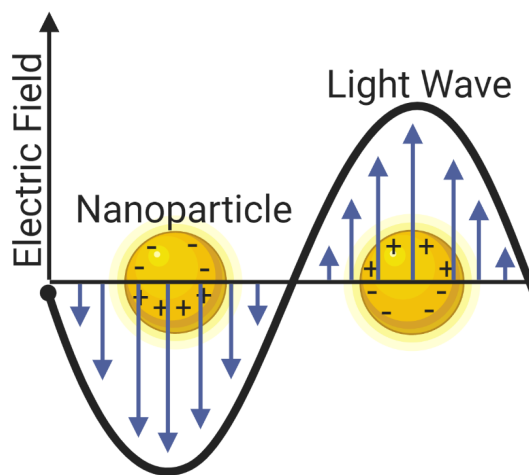


Figure 1.4: Schematic illustration of different electron processes that occur when an Au NP is illuminated with light

power thus rendering the treatment minimally invasive. They are also good photo absorbers and demonstrate good stability under physiological conditions. Research shows excellent thermal ablation of tumor cells by gold nanospheres[12, 13, 14] and nanorods[15, 16, 17] highlighting the effectiveness of NP-based therapeutic methods, this has prompted further research using NPs with

more complex morphologies.

One drawback to more complex NPs is that most synthesis methods use cytotoxic surfactants such as cetyltrimethylammonium bromide (CTAB).[18] Aside from being cytotoxic CTAB is difficult to completely remove from the surface of the NPs hindering its ability to undergo biofunctionalization resulting in limited targeting abilities. The incompatibility of CTAB and other similar surfactants has resulted in an intensive search for surfactant-free NP synthesis methods for controlling NP morphology.

1.5 NIR Region

For heating of the NPs to occur, it is essential that the light-to-heat conversion response is tuned to occur with NIR light. The NIR region has light wavelengths ranging from 750 to 1100 nm. This region is crucial in biological applications as it is here where the maximum penetration of light through biological tissue and skin occurs. To treat deep-tissue-buried tumors using PTTs, it is necessary to use NPs which absorb light in the biological windows I (700–950 nm), and II (1000–1350 nm). This allows maximum conversion of incoming light into heat.[19] (Figure 1.5 and 1.6). The absorbance band of the NPs is tunable allowing NPs to be designed with an absorption in the NIR region for optical applications.

1.6 Imaging NPs inside the body

Multi functionalized NPs have the ability to be used for real-time visualization inside the body.[22] Initially this was achieved using fluorescence imaging but recently Raman imaging has emerged as an attractive alternative option. Raman scattering gained popularity because it could be efficiently excited and detected within the NIR optical window. It is also less sensitive to photobleaching when compared to fluorescence imaging techniques. [23, 24] One main disadvantage of using Raman imaging was the weak intensity of the Raman signal. This was resolved by using Surface Enhanced Raman Scattering (SERS) where the strong light induced electromagnetic fields amplified the Raman signal 8-10 orders of magnitude. [25]

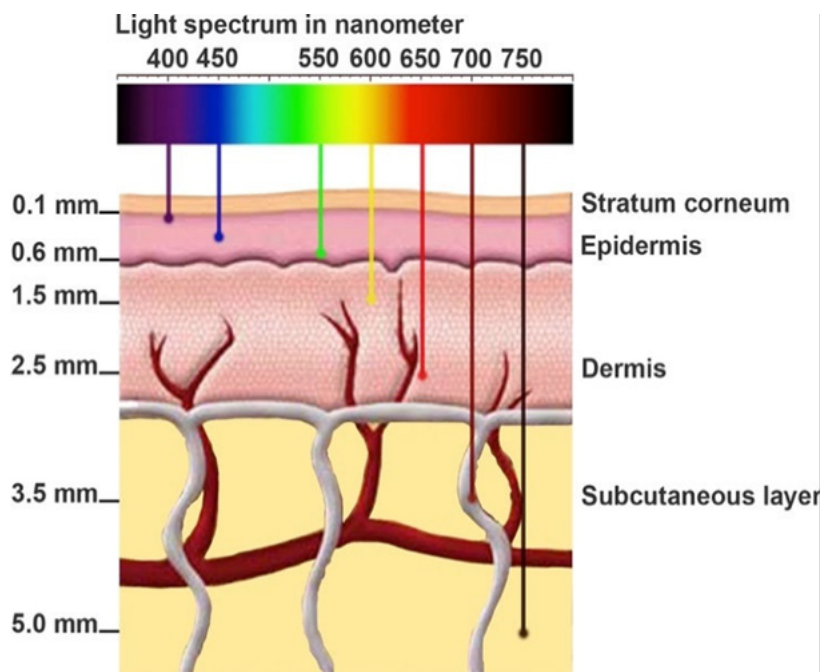


Figure 1.5: Spectrum of light demonstrating the biological optical window in the NIR region. Image shows maximum penetration of light at 750 nm up to 5 mm .Reprinted from "Opportunities and challenges of fluorescent carbon dots in translational optical imaging" [20]

1.6.1 SERS

SERS on metal NP surfaces is extremely popular as there is interaction of the NP with the incident light photon. This interaction creates an enhanced electromagnetic field around the metal surface. As a result, Raman target molecules present in this vicinity show enhanced Raman scattering. Therefore, by functionalizing NPs with the right Raman target molecules, we can image and track the NPs location inside the body using SERS.

1.7 Photothermal Standardization

At present, the measurement of the thermal output generated by NPs is not standardized and a number of different methodologies are employed to screen their light-to-heat conversion efficiencies. There is little consistency between the measurement methods and the accessibility of some of the methods are limited. Lack of standardized measurements across the field makes it particularly difficult to replicate the work of other researchers and more rapid standardized tests are required.

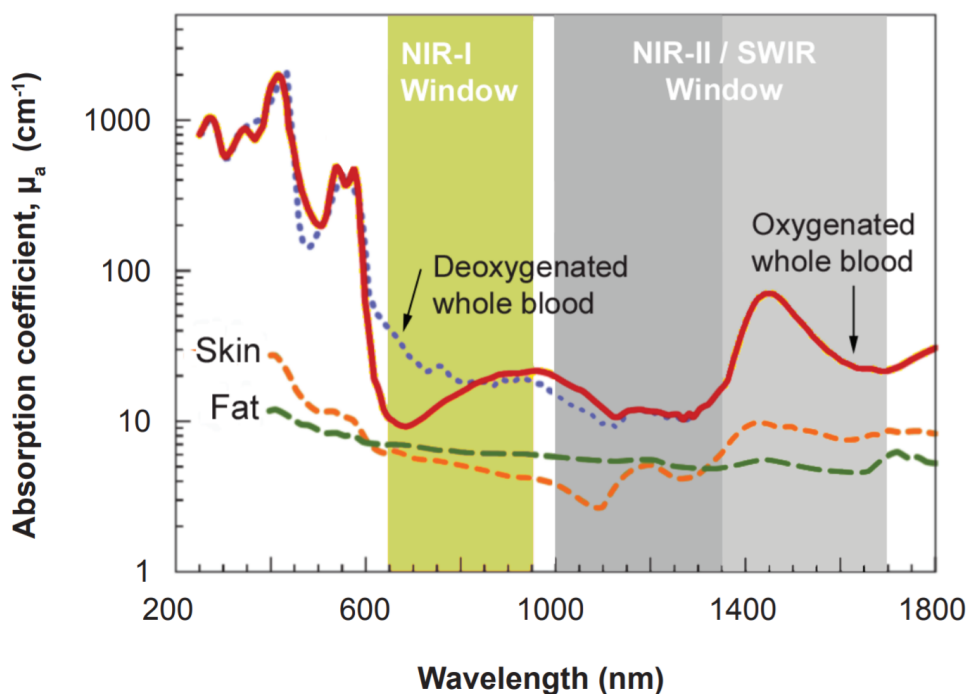


Figure 1.6: Spectrum of light demonstrating the absorption coefficients of 4 different biological components in the NIR region with NIR Window 1 and 2 (aka Short Wave Infrared Window). Reprinted from "Review of biomedical applications of contactless imaging of neonates using infrared thermography and beyond" [21]

The many different approaches make interpreting the thermal output difficult to extrapolate to in-vivo experiments. Establishing a relationship between benchtop and in-vivo measurements is of great importance, as it will allow for the rapid pre-screening of metallic NPs light-to-heat conversion efficiency prior to carrying out experiments in animals.

1.8 Current Approaches Measuring Photothermal Output: In-Solution, In-Vitro and In-Vivo

Researchers have studied the PT properties of NPs using a variety of different approaches, extending from theoretical modeling through to in-vivo measurements. However, it is uncommon that researchers detail the whole process; many go straight to application without prior screening of the PT efficiencies of their NPs. Those that do screen their NPs do not employ standardized

methods making it difficult to compare the properties of NPs used in 2 different studies. Lack of standardization arises due to some screening methods being very complicated and as a result they are difficult to replicate on an everyday basis.

Yuan et al [26] has developed a theoretical model for prescreening gold NS. The group have created AuNS models developed using TEM images acquired from different batches of NS. The model adjusts the arms of the NS to maximize inter-branch distance and also dielectrically functionalizes the particles to replicate the properties of the Au in water. These AuNS were then meshed together to provide good spatial density and incrementally rotated by 30°. This was done to randomize the orientation of the branches relative to the z-polarized incident field. The theoretical absorption spectra were averaged to account for the orientation dependence of the NS on the electric field. Finally, the modeling and experimental results were compared. The maximum absorbency for both cases was the same but the peak widths did not match. There was significant broadening of the experimental bands compared to the theoretical. The NS were then used for photoluminescence imaging and proven to be effective contrast agents for biological applications.

Unlike the above group, Govorov et al [27] used a more experimental pre-screening approach (Figure 1.7) for testing NPs. The researchers embedded AuNPs in a matrix of known thermodynamic properties such as ice and then placed the sample in an isolated chamber. A thermocouple was pinned inside a well that contained the ice. This apparatus was placed in a Peltier Cooler within a nitrogen-controlled climate box which was then placed under a Raman/near-field scanning optical microscope. A reference sample of ice without NPs was put into the chamber and used as a control. The ice was then excited using a 532 nm laser. It was observed that the sample of ice containing NPs melted resulting in the formation of a crater whereas no melting occurred in the control even at the highest laser intensity. While this method is novel for measuring the PT output from NPs, its' intricate design does not lend itself to frequent and rapid screening of NPs and their heat conversion properties.

Other groups like Gonzolo [28] have developed simpler methods for prescreening their NPs. They placed their synthesized 10 gold nm spheres in a quartz cuvette and irradiated the cuvette

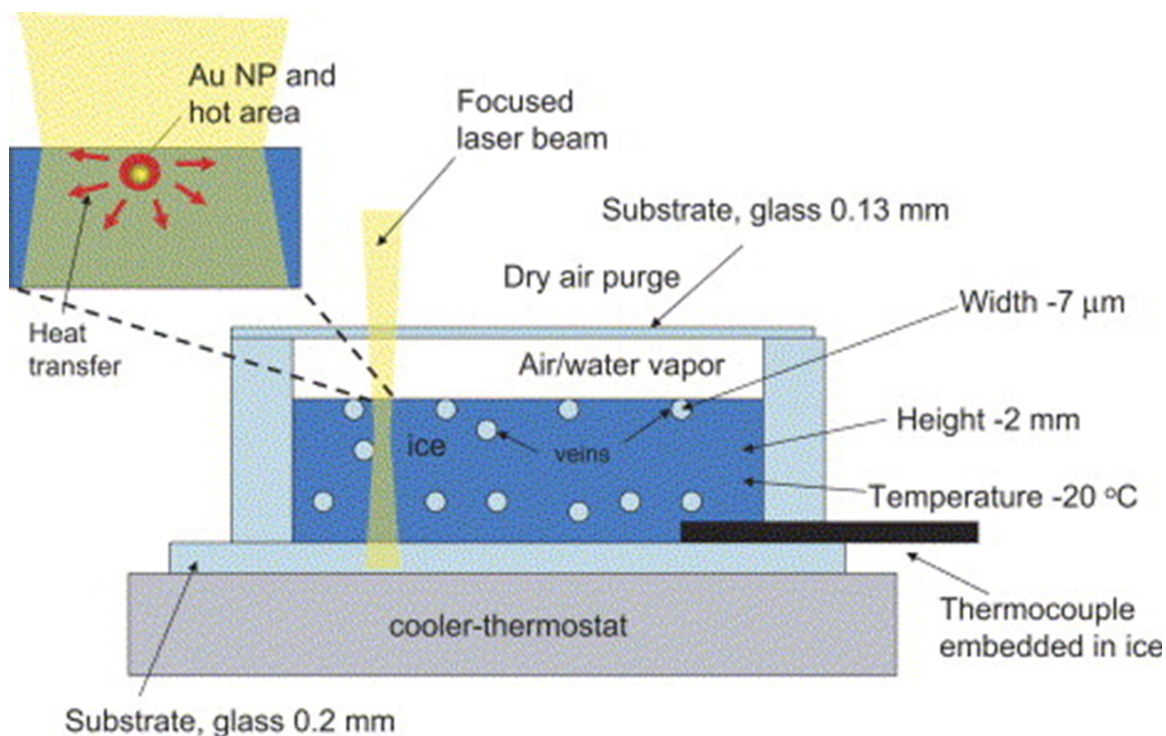


Figure 1.7: Image represents setup used by Govorov et al, wherein NPs are embedded in ice in a glass chamber. A thermocouple is also embedded to record temperature changes. A focused laser beam is used to heat the NPs. Reprinted from "Generating heat with metal nanoparticles"[27]

with a 975 nm laser. The temperature increase of the sample was measured using a thermocouple that was dipped into the sample prior to irradiation. The spheres provided a heat increase of 5.5 °C. They then performed in vitro studies after creating a nanocomplex using up-conversion nanoparticles (UCNPs) and used the 10 nm spheres on breast cancer cells.

Another similar approach is used by Yilong and group [29] used tungsten oxide nanorods with SPRs ranging from 400 to 1200 nm. They created nanorod solutions of various concentrations (0-1000 µg/ml) and irradiated them with a low power 980 nm NIR laser for 10 mins. They used a thermocouple to record temperature change of the solutions every second and calculated efficiency of heating. They also performed cytotoxicity and in vitro tests on cancer cells. Other groups have opted to bypass the pre-screening of NP thermal properties.

Leslie et al.[30] evaluated PT using gold nanocages which were 65 nm diameter with a maximum absorption at 800 nm. They however did not prescreen their NPs and directly incubated

with breast cancer cells and irradiated them. They measured cell damage as a result of power and duration of laser exposure. The percentage of dead cells increased with increasing exposure time up to 5 min and then became steady.

Huang and group [12] also adopted a similar strategy using nanospheres. The spheres were 30 nm in diameter with a maximum absorption of 530 nm. They incubated the nanospheres with cancer cells and characterized the effectiveness of the NPs by the amount of power needed to destroy the cells. They observed that cancer cells containing NPs were destroyed with 20 times lower laser energy power than that required for the destruction of cancer cells not containing NPs.

Other researchers like Bucharskaya et al [15] and Erin et al [23] directly used animal models to test the effectiveness of their NPs. Bucharskaya et al [15] created gold nanorods of approximately 42 ± 8 nm in length and 10 ± 2 nm in diameter. They were injected at different dosages into rats with liver cancer. The rats were divided into 3 groups and given varied dosages of nanorods. The first group of rats was given one dosage, the second group was given two dosages and the last group was given three dosages. The nanorods were left to incubate for a day inside the rats. The rats were then irradiated with an 808 nm laser for 15 mins. It was observed that rats with the highest nanorod dosage demonstrated the largest increase in localized temperature and as a result a greater number of cells had undergone necrosis.

Erin and group [23] also created nanorods and tested them on mice having tumor growth. These nanorods had a SPR of 800 nm and were delivered to the tumor sites both intravenously and through direct injection. In vivo tests were performed on these mice using a small, portable, continuous wave NIR laser of 808 nm. Significant decrease in mice tumor size was observed when a power of 1.7-1.9 W/cm² was applied for 10 mins. Inhibition of tumor growth for both delivery methods were observed over a 13-day period.

The research objectives of this work have been highlighted below:

1. Develop a simple, user-friendly laser-facilitated heating system and measure the PT conversion efficiency of NP solutions.
2. Evaluating the heat output and heating properties of generated gold NS and NPr upon irradi-

ation with a laser.

3.Measuring SERS signal generated from the NPs functionalized with different Raman reporters that can be used for elucidating the NPs location when inside the body.

2. MATERIALS AND METHODS

2.1 Materials

All chemicals were purchased from Sigma-Aldrich (St Louis, MO). All chemicals were used as received without further purification. De-Ionized (DI) water was used in all experiments. All glassware was cleaned with soap and water, rinsed with DI water followed by acetone, and stored at 150°C before use. In between different experimental trials the quartz cuvette was cleaned in a bath of freshly prepared aqua regia (HCl/HNO₃, 3:1 v/v) and then rinsed thoroughly with DI water.

2.2 NP Synthesis

Literature showed that simple morphologies of Au like nanospheres and nanorods were extremely popular for PTT. We however focused on more complex morphologies for the same application. Due to the high toxicity of surfactants like CTAB, our study also focused on those NPs whose synthesis methods were surfactant free. One such NP with good homogeneity and proven effective heating properties was AuNS (gold nanostars). These NS were prepared using a seed mediated procedure where arms of different lengths were grown using spherical NP seed templates. Similar to the NSs, surfactant free methods were explored for the synthesis of gold nanoprisms (AuNPrs) as well. Both sets of particles were also chosen due to the tunability of maximum absorbency around the NIR region of the electromagnetic spectrum, making the applicable to PTTs.

2.2.1 Gold nanosphere (seed) synthesis

Spherical AuNP [31] or seeds of approximately 30 ± 5 nm were synthesized via citrate-reduction of auric acid. In a typical synthesis, 15 mL of 1% trisodium citrate solution was added to 100 mL of boiling auric acid solution (1mM) whilst stirring vigorously. The heating and stirring was maintained for 30 mins, after which point the NPs were allowed to cool to room temperature. Successful synthesis was determined via a color change from light yellow to red. For long-term storage the AuNPs were placed in a refrigerator at 4 °C , and used for a period of 6 months before fresh particles were synthesized.

2.2.2 Gold nanostar (AuNS) synthesis

AuNS were synthesized according to a seed mediated procedure [31] (Figure 2.1), which yielded NSs with an absorbance of 820 nm. According to the procedure, 100 μ L of AuNP seed solution, 10 μ L of HCl (1 M) and 10 mL HAuCl₄ (0.25 mM) were combined in a beaker. Under moderate stirring, 100 μ L of AgNO₃ (0.5 mM) and 50 μ L (100 mM) ascorbic acid were added simultaneously to create AuNSs. Successful synthesis of AuNSs was indicated by a color change of the solution from red to blue/green. To shift the SPR of the NS close to the laser frequency, different volumes and concentrations of some of the reagents were experimented with. 2 different volumes of seed solution (100 μ L and 200 μ L) was used. To each seed volume, 4 different concentrations of AgNO₃ (5 μ M, 30 μ M, 0.5 mM and 30 mM) was added keeping concentrations and volumes of other reagents constant. UV-vis-NIR spectroscopy of all 8 samples was taken and compared. 40 μ L of 5% Citrate solution was added to each sample to avoid aggregation and maintain stability.

2.2.3 Gold Nanoprism (AuNPr) Synthesis

The first method of AuNPr synthesis yielded NPrs with a SPR of 950 nm.[32] To prepare these NPrs, 100 mL of HAuCl₄ (2 mM) and 120 mL of freshly prepared Na₂S₂O₃ (0.5 mM) were mixed, under mild stirring for 9 mins. To this mixture, 20 mL of Na₂S₂O₃ (0.5 mM) was further added and allowed to sit for 1 h. This reaction saw a color change of the mixture from light yellow to dark brown indicating the formation of NPrs. TEM images and UV-vis-NIR spectra was taken of the samples to check for homogeneity among NPs.

The second procedure used was described by Gabriel and group.[33] (Figure 2.2) The synthesis was performed as described but with reaction volumes reduced by 10 times. 2 beakers ('A' and 'B') each containing a mixture of 3 μ L of KI (0.1 M) and 11 mL of Na₂S₂O₃ (0.5 mM) were made. Beaker 'A' was first mixed with 20 mL aqueous auric acid (2 mM). Addition of 'A' to the auric acid resulted in an instantaneous color change from yellow to light brown. The solution was then allowed to rest for 4 mins before beaker 'B' was added. The second addition saw a further color

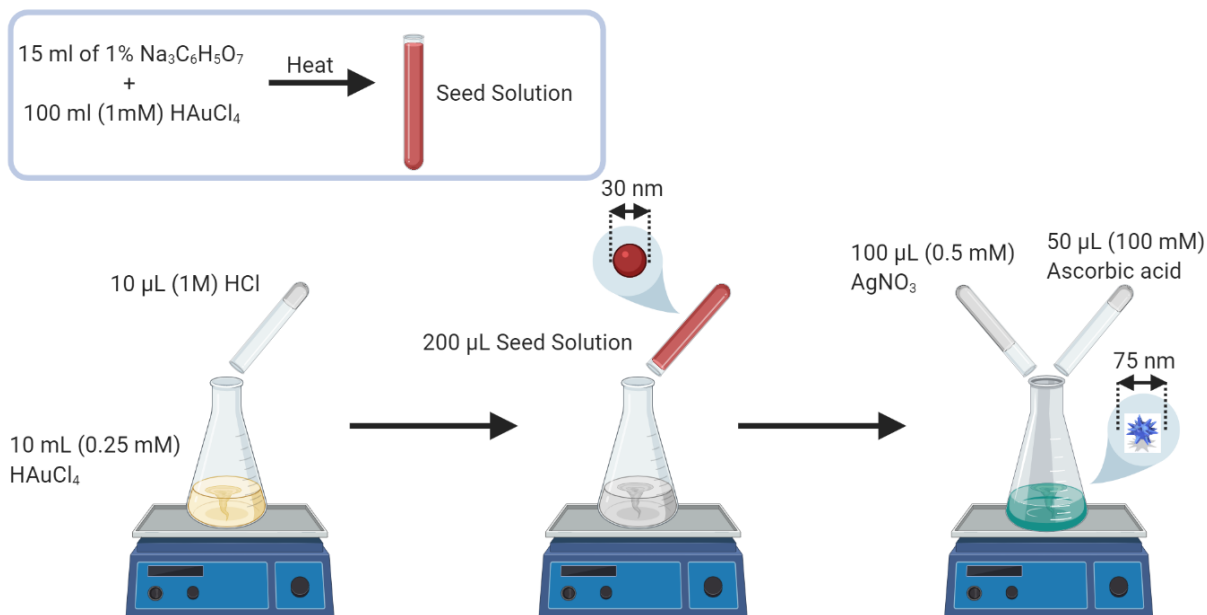


Figure 2.1: AuNS Synthesis protocol developed from the seed mediated procedure yielding a blue-green mixture of NSs with an absorbance at 820 nm

change to dark brown which occurred gradually over a further 4 mins. The mixture was allowed to rest for a further 4 mins before 7 mL of $\text{Na}_2\text{S}_2\text{O}_3$ (0.5 mM) was finally added to the mixture to yield a dark brown mixture indicating the formation of the NPrs. TEM images and UV-vis-NIR spectra were taken of the samples to check for homogeneity among NPs.

2.3 Characterization Techniques

The NPs were characterized using UV-vis-NIR spectrometry using a Cary 60 UV-vis-NIR Spectrometer (Resolution: 1.5 nm, wavelength range: 190 – 1100 nm). The morphology of the NPs was characterized using JEOL 1200 EX TEM operated at 100 kV. 8 μL of the NP solution were immobilized on a carbon-coated Cu grid for TEM analysis.

2.4 Heating Setup for prescreening

Our heating approach is a cuvette-based approach where the sample is placed in a cuvette and subjected to laser irradiation. The heat increase was measured using a temperature measurement

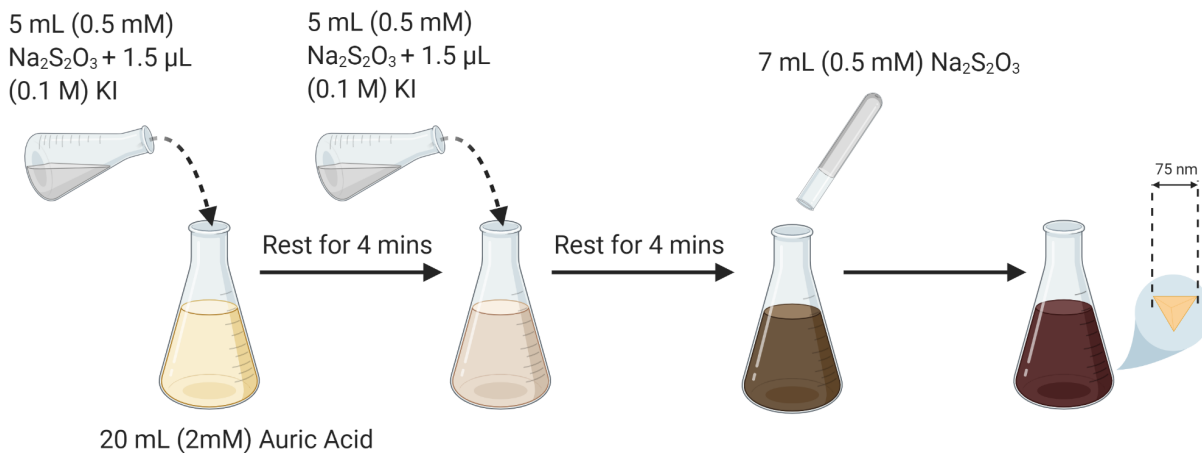


Figure 2.2: AuNPr Synthesis protocol yielding a brown mixture of NPr with an absorbance at 1000 nm

device. Four different thermocouples were tested to determine the accuracy of the temperature readout. The thermocouple was connected to an Arduino micro-controller to enable automatic logging of the NP solution temperature to a computer for easier analysis.

2.5 Temperature measurement device

For our application, we were searching for a temperature measurement device that was accurate between the temperature ranges of 20 to 50 °C. To decide on a suitable temperature measurement device, 4 different temperature sensors were tested (Table 2.1). Sensor 1 was a K-type thermocouple from HiLetGo. It had a resolution of 0.25 °C. Sensor 2 was a thermistor from GodShark with a resolution of 1°C. Sensor 3 was a K-type thermocouple from Adafruit with a resolution of 0.25 °C and Sensor 4 was also a K-type thermocouple from Wiltronics with a 1°C resolution. These sensors were individually submerged in conical flasks containing 200 mL of water at room temperature. The conical flask was placed on a hot plate and the water was heated for 30 mins. During heating a lab thermometer was also placed in this flask to measure temperature increase of the water sample. The temperature sensors being tested were wrapped around the lab thermometer to measure the temperature at the same location. Temperature measurements were taken every min for 30 mins from the sensor and compared with the lab thermometer reading to test for accuracy.

[34, 35].





Type of measurement system	Image	Brand	Accuracy	Range
K-Type Thermocouple (Sensor 1)		HiLetGo	0.25 °C	0 to 400°C
Thermistor (Sensor 2)		GodShark	1 °C	0 to 300°C
K-Type Thermocouple (Sensor 3)		Adafruit	0.25 °C	0 to 500°C
K-Type Thermocouple (Sensor 4)		Wiltronics	1 °C	-40 to 250°C

Table 2.1: Comparison of 4 different sensors tested for accuracy

2.6 Temperature data processing

The temperature measurement device was connected to a microcontroller via a breakout board supplied by Adafruit. Temperature changes were measured using a change in voltage between the 2 metals at the thermocouple junction. The difference in voltage was uploaded to the microcontroller board. Open source software PLX-DAQ was used to automatically transfer the microcontroller output from the serial monitor of the Arduino microcontroller IDE to MS Excel.

2.7 1064 nm laser system

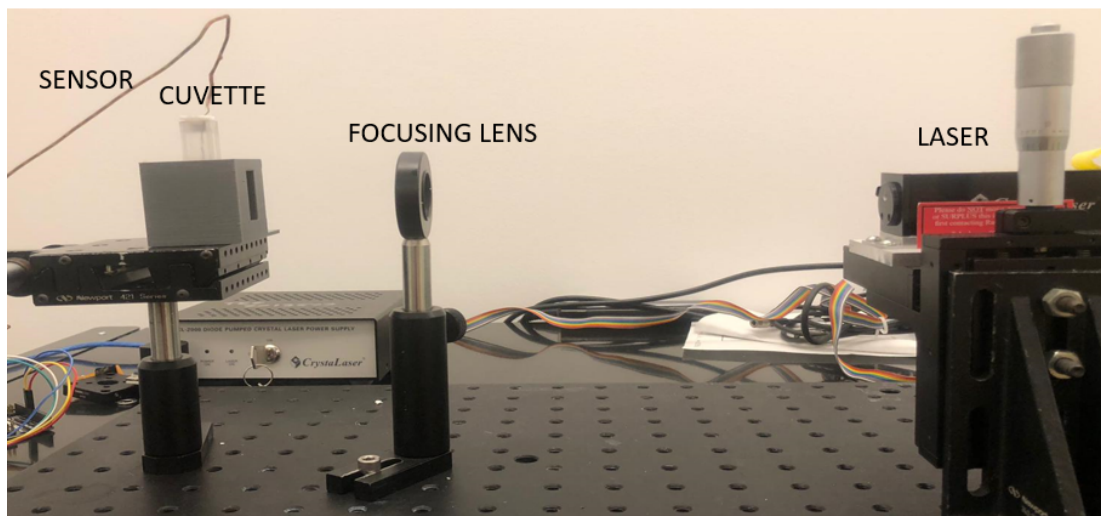


Figure 2.3: Image of the initial 1064 nm laser system screwed onto an optical table. Focusing lens placed at an optimal distance allowing a sharp laser spot in the middle of the cuvette. Temperature sensor inserted into the cuvette from the top to measure sample temperature.

Our initial heating approach used a continuous wave 1064 nm laser (Figure 2.3). It had an unfocused power output of 165 mW/cm^2 and a focal length of 30 cm. The laser was first mounted onto an x and y translational stage. The focus point of the laser was optimized using a laser power meter to locate the distance at which the laser light had maximum intensity and was a point source. In our case the focal length of the laser, transmitted through a focusing lens was 30 cm from the laser source. A cuvette holder was designed and 3D printed using acrylonitrile butadiene styrene (ABS) to hold the cuvette in place on the optical stand. A thermocouple was inserted into the cuvette from the top to measure heat increase. The thermocouple was also connected to a microcontroller which was used to process the output from the temperature sensor.

2.8 785 nm laser system

Our second system incorporated a more compact and efficient heating system using a 785 nm probe laser. This system also allowed us simultaneously measure SERS signal intensity and heat

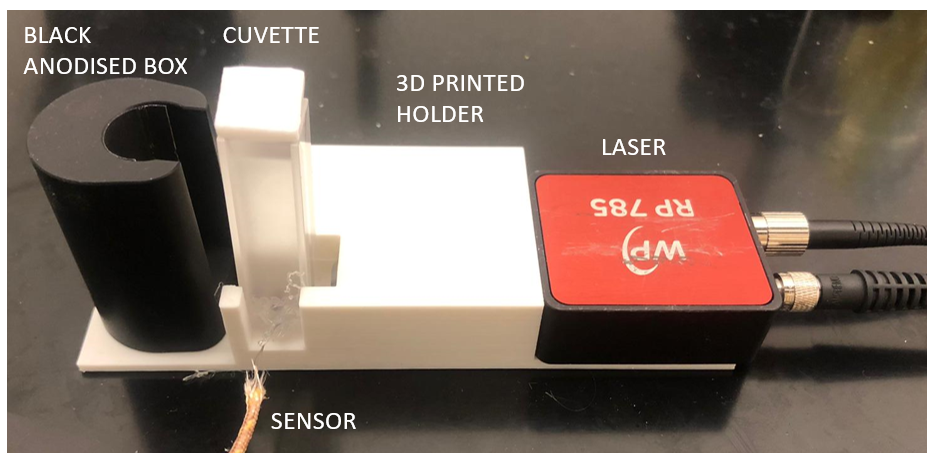


Figure 2.4: View of the 785 nm laser system designed to measure heat output from the sample in the cuvette using a thermocouple. Black anodised box present behind the cuvette and prevent background noise for SERS Enhancement

output during a heating cycle.

The 785 nm system (Figure 2.4) consists of a fiber optic continuous wave laser with a maximum unfocused laser power output of 300 mW/cm^2 and has a focal length of 1.1 cm. A 3D printed holder was designed using polylactic acid (PLA) to hold the laser and cuvette together. The 3D printed holder features a cuvette insert. The holder is designed so that the laser is focused 5.5 mm above the center bottom of the cuvette. To make sure the thermocouple was in an identical position for each measurement, a 1 mm diameter hole was drilled onto the bottom side of the cuvette. This allows the thermocouple to be inserted and fixed into position using super glue. A cap was placed at the top of the cuvette to avoid any evaporation of sample during the experiments. To verify this, the cuvette was measured using a balance before and after heating during which there was negligible change in volumes. Behind the cuvette was a black anodised box which was used to absorb any excess laser light exciting from the back of the cuvette. This was also used to reduce background spectra for SERS enhancement.

In a typical thermal measurement, the cuvette was first cleaned with aqua regia and rinsed with DI water. $100 \mu\text{L}$ of NP solution was placed inside the quartz cuvette ($700 \mu\text{L}$ – total volume) and the cap of the cuvette was inserted to prevent evaporation. The microcontroller was then connected

to the computer. Once the reading had stabilized, sample temperature was measured and treated as a baseline and the laser was turned on. Temperature readings were collected every second and stored in MS-Excel. This was done for a period of 20 mins after which the laser was switched off. The cuvette was allowed to cool and was cleaned before the next measurements were taken. Temperature readings were averaged for every minute to smoothen the data.

2.9 Heating Experiments

To better understand the heating properties of the NPs, different experiments were conducted. To start off, the stability of the NPS were tested over a period of 1 day.

2.9.1 Stability of NPs

This experiment was performed to check the stability of the NPs after they were created and stored overnight in the refrigerator at 4 °C. Absorption spectra and heat output were used to characterize stability of the NPs.

Method: 10 mL of AuNPs were generated from the above described method. 100 μ L of NP sample was taken out and the UV-vis-NIR spectra was obtained. This sample was then heated for 20 mins (300 mW). The remaining sample was stored overnight in the refrigerator at 4 °C. The next day 100 μ L of NP sample from the refrigerator was taken out. This sample was analysed using the UV-vis-NIR spectroscopy and heated for 20 mins in the laser system (150 mW/cm²). At this time, our NS synthesis procedure was still in development thus yielding NS with an absorption wavelength around 700 nm.

2.9.2 Effect of Citrate buffer on NS solution

To further stabilize the NS and to help avoid aggregation, additional amounts of a 5% citrate buffer was added. This experiment was performed to look at changes in the spectra and stability of the NSs when capped with and without the citrate buffer. The above experiment was not performed on the NPrs as they were stable after creation and had no need of a stabilizing agent.

Method: Two samples of freshly prepared NSs were used. One sample (Sample A) was left to be while the other (Sample B) was capped with a 5% citrate buffer. UV-vis-NIR spectra of both

NSs were taken every day for the first four days and then once on the seventh day

2.9.3 Effect of volume on heat output

This experiment was conducted to observe the impact volume of the sample had on the heat output. The procedure mentioned below was first conducted on the AuNS solution and repeated for AuNPr. All experiments were first performed in the 1064 nm system and then on the 785 nm system. The experimental methodology remained the same for both setups

Method: 10 mL of AuNS/AuNPr was synthesized from the above protocol. This batch was divided into 3 samples with volumes of 300 μL , 200 μL and 100 μL . 300 μL of solution was first placed in the cuvette of the 1064 nm system. The cuvette was covered from the top using the cuvette top to avoid evaporation of the sample. The laser was turned on (full laser power, 150mW/cm²) and the heat output was noted from the temperature probe. After 20 mins of heating the laser was switched off and the sample was discarded. The cuvette was cleaned with DI water multiple times before repeating the method again with 200 μL and 100 μL of the sample. Another batch of AuNS/AuNPr solution was prepared and divided into 3 samples with volumes of 300 μL , 200 μL and 100 μL . 300 μL of solution was placed in the cuvette in the 785 nm setup. The cuvette was covered with it's top to avoid evaporation. The laser was turned on (full laser power, 300 mW) and the heat output was noted. After 20 mins of heating the laser was switched off and the sample was discarded. The cuvette was cleaned with DI water multiple times before repeating the method again with 200 μL and 100 μL of the sample.

2.9.4 Change in NP morphology: before and after heating

In this experiment we wanted to establish whether the laser-induced heating of the NPs had any effect on the particle morphology. AuNS consist of spherical cores surrounded by arms which grow anisotropically. The length of the arms is elongated with the addition of HCl during the preparation protocol.[31] Arms of greater lengths cause the absorbance of the NSs to shift towards the NIR region. Modulating the extension of the arms means that the absorbance frequency of the particles can be matched to the laser frequencies (785 nm) being used in the experiments.

The AuNP solution consisted of triangular plates of multiple different sizes. Unlike the NS, the NP solution was not a homogeneous mixture consisting of just the NPs. There was also a lot of spherical byproducts that were created as a result of the reaction.

Method: 10 mL of AuNPs were generated from the above described method. 40 μL of 5% citrate solution was added to stabilize the AuNSs. 8 μL of NP sample was taken out before heating for imaging using the TEM and the UV-vis-NIR spectra was obtained. Heating was performed on the sample for 20 mins (300 mW/cm²). After heating 8 μL of the sample was again taken out for TEM analysis and a UV-vis-NIR spectra was obtained as well.

2.9.5 NP exposure to multiple heat/cool cycles

This experiment was performed to establish heat output curves generated by the NPs when subjected to three heat/cool cycles. This experiment was performed on both AuNS and AuNPs.

Method: NPs were generated from the above described procedure. 100 μL of NPs were placed in the cuvette. The NP were subject to 20 mins of laser light exposure after which the laser was turned off for 15 minutes, allowing the sample to cool down. The samples were then re-exposed to the laser for 2 more 20-min heat, 15-min cool cycles. The length of heat and cool cycles were chosen based on the temperature plateauing after exposure through a trial and error method

2.10 SERS Enhancement

SERS is a very powerful tool for imaging, tracking and identification of molecular species inside the body.[36] SERS on metallic NP surfaces is extremely popular as there is interaction of the NP with the incident light photon when a Raman reporter is attached to the surface. In our application, we are looking at SERS Enhancement of the NS and NPs for 2 Raman reporters namely 4-mercaptobenzoic acid (MBA) and 1,4-Benzenedithiol (BDT).

MBA has vibrational bands that are extensively characterized using Raman spectroscopy.[37] Different concentrations of MBA were created by dissolving in ethanol.[38] Concentrations ranged from 1×10^{-2} M to 1×10^{-8} M. 100 μL of each solution was added to 1 mL of NP solution, thoroughly mixed and left to incubate for 1 h. After incubation, the absorption spectrum of the

modified NP solution was compared with a control containing only the bare NP solution to find the correct concentration. A similar process was followed for the BDT Raman reporter.

2.10.1 SERS Enhancement Procedure

Identical procedures were used to acquire SERS spectra from the NS and NPr. The NP were analyzed using the 785 nm Raman probe system. Initially, a Raman spectrum of the NP solution without the laser switched off was taken and treated as the background. We observed some background spectra here due to the material of the cuvette holder. To remedy the interference the 3D print material used to construct the cuvette holder was switched from ABS to PLA as PLA exhibited minimal Raman scattering. A slight alteration was then made to the cuvette holder design involving the partial removal of the holders back wall and the additional use of an external black box to absorb the extra radiation emitted out from the back of the cuvette. (Figure 2.4) NP samples were heated using the 785 nm laser with the new cuvette setup for 20 mins. A Raman spectrum was collected every 5 mins to observe changes in spectra. Simultaneously the heat output from the NP was also being captured. These were taken every second and averaged for every min. The peaks analyzed from the modified NPs were at wavenumbers of Raman shift= 1081 cm^{-1} and 1591 cm^{-1} . [39, 40, 41] The Raman peaks were baseline corrected and plotted in MATLAB whereas the heat output was captured in excel and plotted in python.

3. RESULTS

3.1 Temperature Measurement Device

Figure 3.1 gives the results of the probe accuracy testing (probe details given in Table 2.1). The glass braided K-type thermocouple (Figure 3.1, bottom left, sensor 3) provided the best overlap between the thermometer and temperature probe readings. This thermocouple also had a small head making it ideal for small sample sizes (e.g., $<200 \mu\text{L}$). Other thermocouples exhibited variation in the measured temperature when compared to the thermometer values.

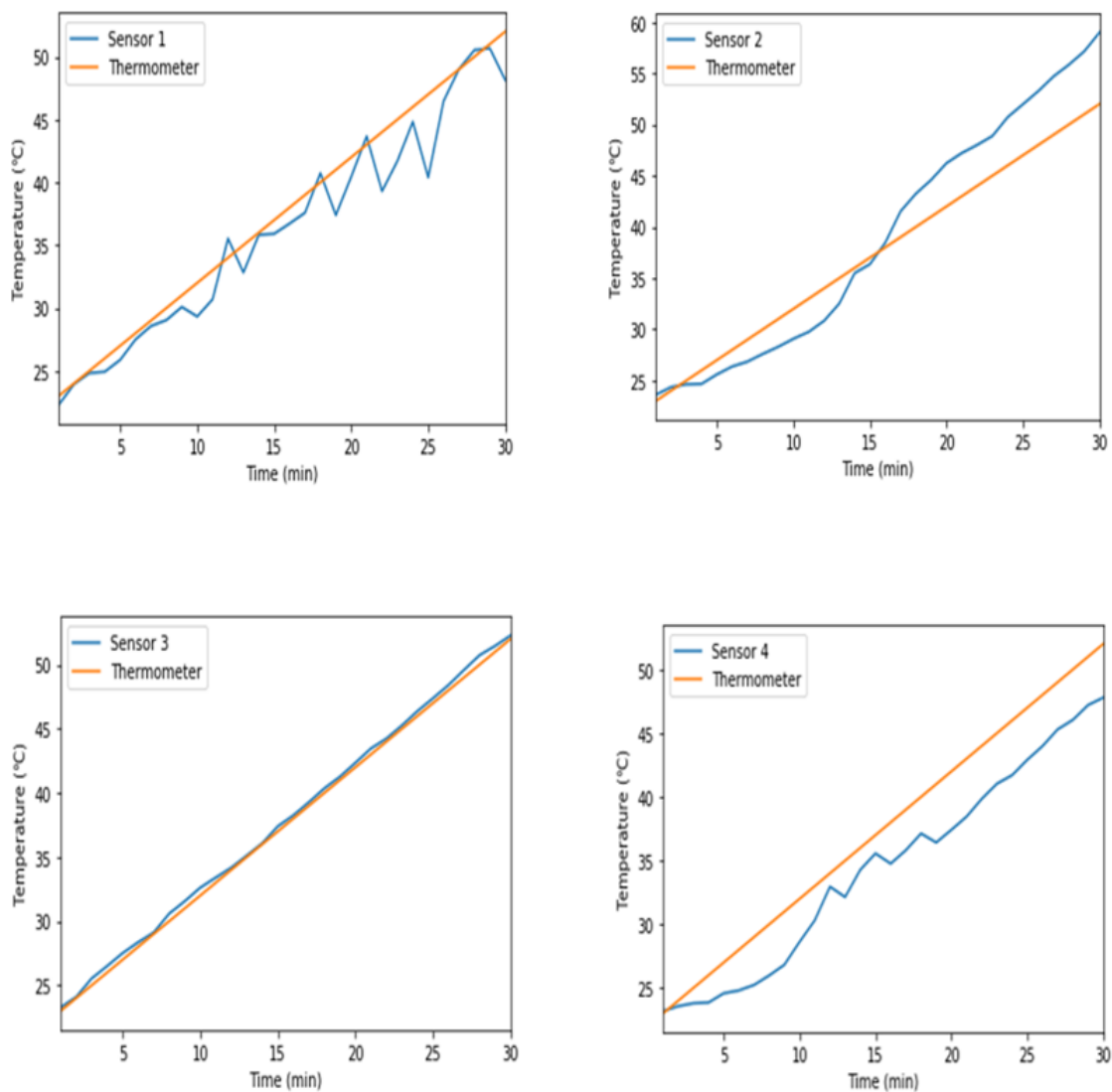


Figure 3.1: Testing results for sensor 1,2 ,3 and 4 (data provided in Table 2.1) samples were heated at a rate of $0.865^{\circ}\text{C}/\text{min}$. Data comp for 30 mins. Thermocouple measured samples were compared with a calibrated mercury thermometer (Orange)

3.2 Characterization of Gold nanospheres

The successful synthesis of spherical AuNPs were confirmed by a color change of the reaction solution from light yellow to purple/blue to red (Figure 3.2). The UV-vis-NIR spectra results show that the AuNPs have a λ_{max} of 519 nm with an absorbance of 0.88. The TEM image of the NP seed shows that the diameters measure 30 ± 5 nm. The diameters were evaluated using ImageJ.

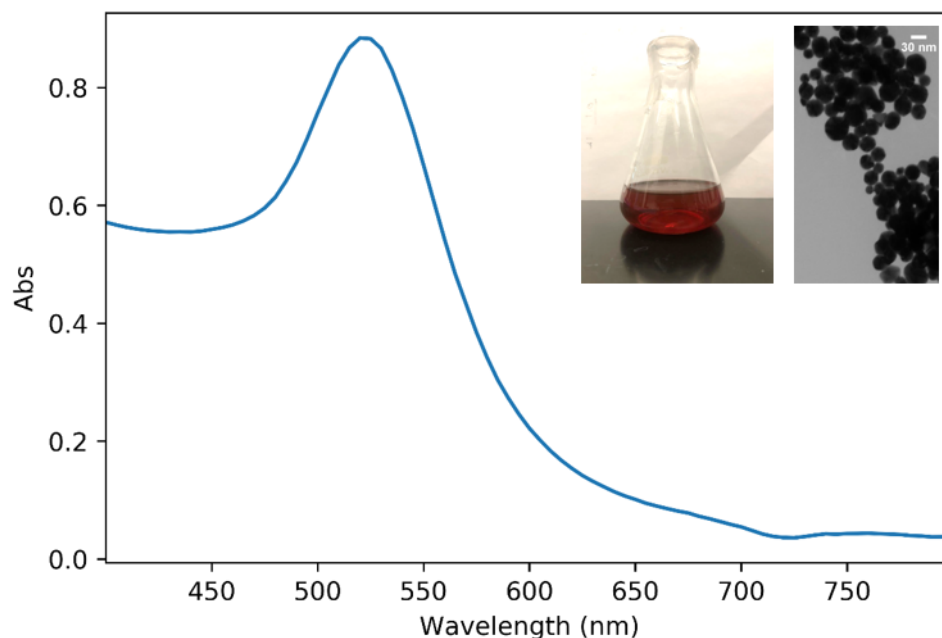


Figure 3.2: Au nanosphere Characterization with a λ_{max} of 519 nm with an absorbance of 0.88. The TEM image of the NP seed shows NPs with 30 ± 5 nm diameters. Sample is wine red in color

3.3 Characterization of Gold nanostar (AuNS)

Successful synthesis of the AuNS could be confirmed visually upon observing a color change of the reaction solution from light yellow to light blue (Figure 3.3). From the UV-vis-NIR spectra the average λ_{max} was found to be 820 nm with an absorbance peak value ranging from 0.9 to 1.2. The TEM image of the NS, showed 75 nm Au spherical cores with multiple sharp arms growing at random orientations. The length of the arms was estimated to be between 15-18 nm.

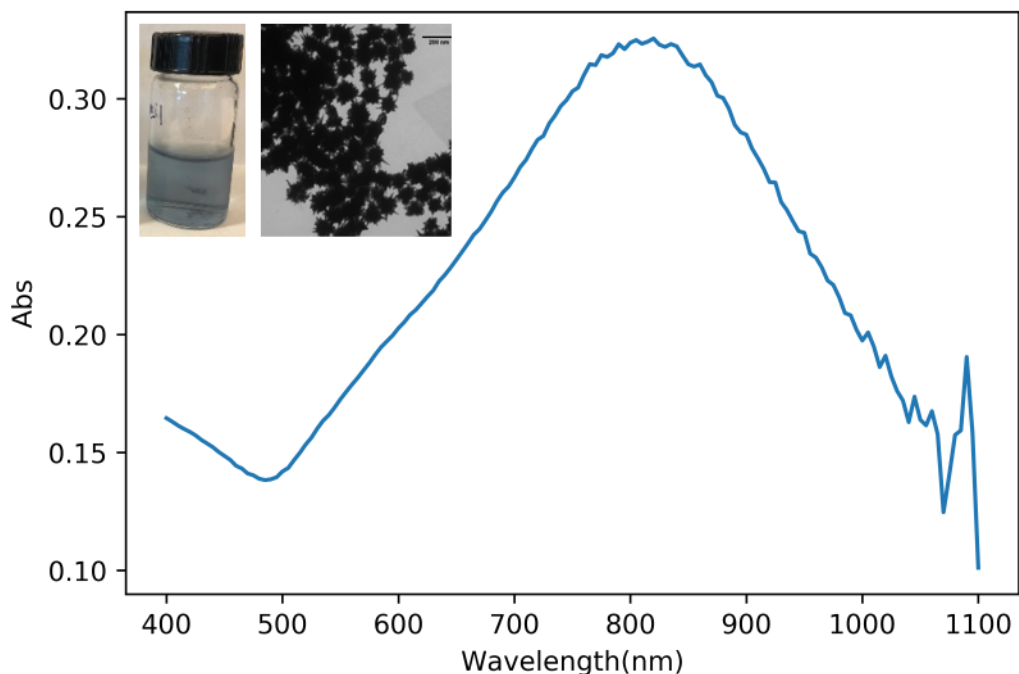


Figure 3.3: Au nanostar Characterization with a λ_{max} of 820 nm with an absorbance of 0.38. The TEM image of the NS shows 75 nm Au cores with 15 nm arms. Sample is light blue in color

3.4 Characterization of Gold Nanoprism

Since most NPr synthesis involves the use of CTAB, we explored surfactant-free synthesis of NPrs without CTAB, however all synthesis attempts yielded a large number of spherical byproducts with only 25-50% of the synthesized batches containing prism shaped particles. The UV-vis-NIR spectra of the NPr showed 2 peaks, 1 corresponded to the length of the AuNPrs while the other corresponded to the height of the prism (Figure 3.4)

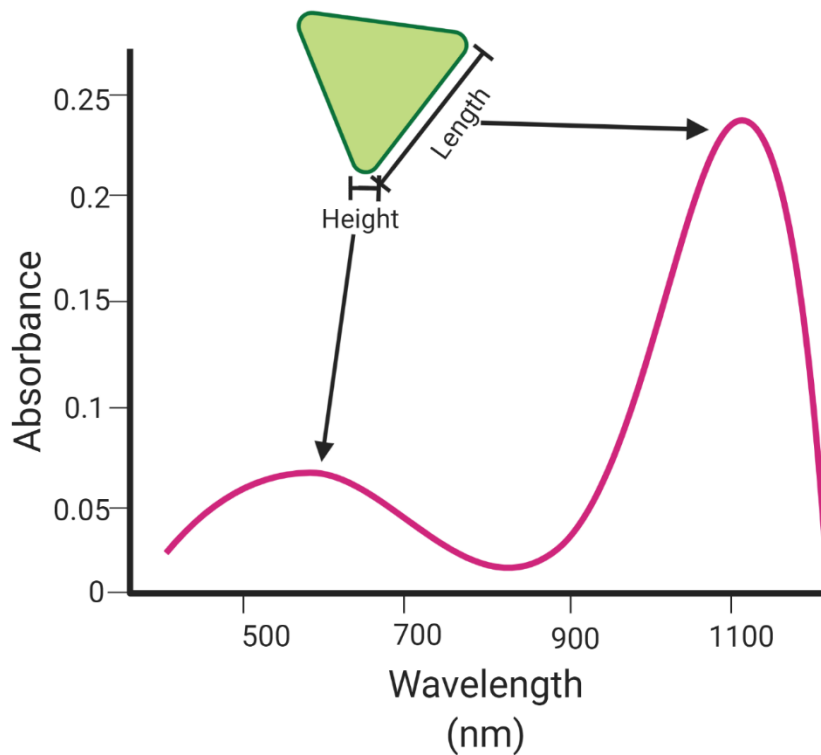


Figure 3.4: UV-vis NIR Spectra of NPRs displaying 2 peaks where one corresponded to the length of the AuNPr while the other corresponded to the height of the prism

AuNPrs generated from Beatriz's method [32] (Method Section 2.2.3) with a SPR of 950 nm was visually confirmed by a color change of the reaction mixture from colorless to brown (Figure 3.5).) The UV-vis-NIR spectrum shows the absorbance wavelengths of the peaks to be 535 nm and 950 nm. The sample was diluted 100 time before measurements were made. The absorbance after dilution at 530 nm was 0.018 and at 950 nm was 0.0273. The TEM image of the AuNPrs showed a heterogeneous mixture of both spherical and triangular shaped particles.

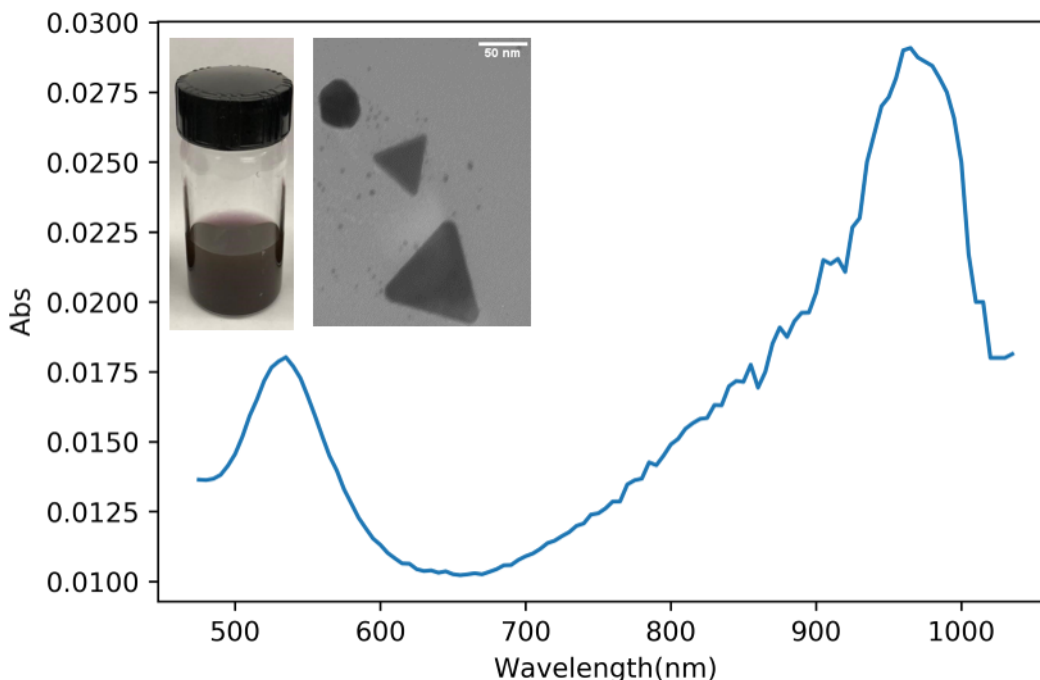


Figure 3.5: Au nanoprism characterization from method1 by Beatriz showing 2 peaks at 535 nm and 950 nm. The TEM image of the AuNPrs showed a heterogeneous mixture of both spherical and triangular shaped particles. Triangular particles had lengths ranging from 40 to 90 nm, while spherical particles had a diameter of 5-30 nm. Sample is dark brown in color

Synthesis of the AuNPrs using the second method by Gabriel and group.[33] (Section 2.2.3) could be confirmed visually upon observing a color change of the reaction solution from light yellow to brown (Figure 3.6). From the UV-vis-NIR spectra of the prisms, 2 peaks were observed at 530 nm and 1000 nm. The sample was diluted 10 times. The absorbance after dilution at 530 nm was 0.0957 and at 1000 nm was 0.1238. Similar to Beatriz's method, this synthesis protocol also resulted in the generation of spherical particles as well as prisms, approximately 25-50% of batches consisted of nanospheres. Using TEM characterization, we could confirm the presence of spherical particles in the mixture with a diameter of 5-30 nm. Centrifuging and then successive washing of the NPrs with DI water lead to aggregation of the particles. We attempted to stabilize the particles with thiol containing chemicals like glutathione and MBA to prevent aggregation during centrifugation but all attempts were unsuccessful.

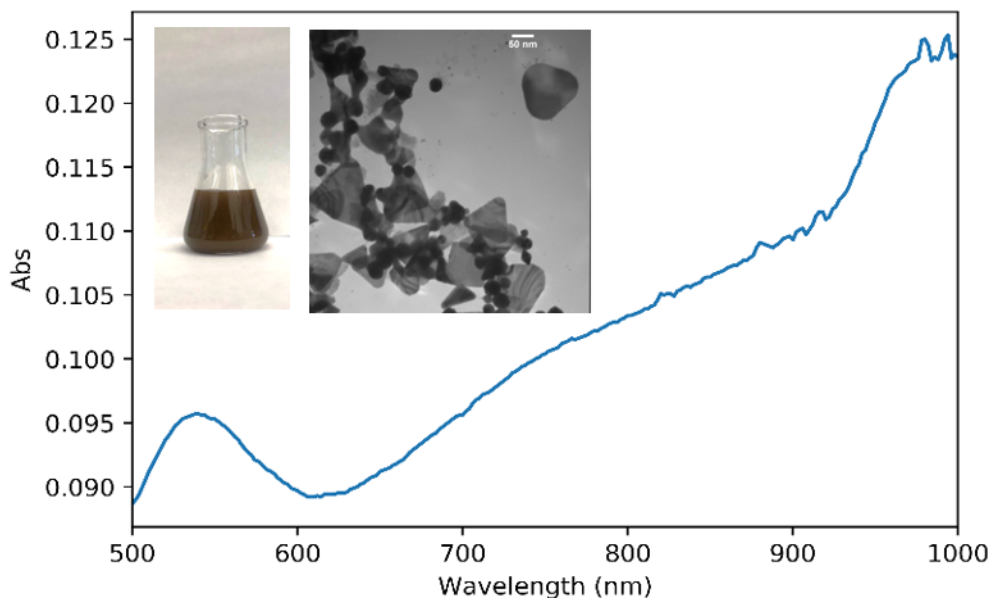


Figure 3.6: Au nanoprism characterization from method2 by Gabriel showing 2 peaks at 535 nm and 1000 nm. The TEM image of the AuNPrs showed a heterogeneous mixture of both spherical and triangular shaped particles. Triangular particles had lengths ranging from 30 to 80 nm, while spherical particles had a diameter of 5-30 nm. Sample is dark brown in color

3.5 Cuvette Based Heating Setup

This method was chosen because of its ease of usage, low cost and simplicity. It was also an approach that could easily be standardized due to a limited number of controls that needed to be maintained throughout the procedure. The addition of a microcontroller to the system allowed automatic logging of the temperature readings to a computer without any human intervention. Our system considerably reduces variation in temperature readings thus resulting in increased reproducibility of measurements.

3.6 AuNS

3.6.1 Overnight storage of NPs and effects on shape and UV-vis-NIR spectra

Though surfactant-free synthesis methods are largely non-cytotoxic, the absence of a strongly adhered stabilizing agent on the surface of the particles can compromise their stability.[42] Hence our brief study which involved comparing the absorption spectra and heat output from the NS on

2 consecutive days was deduced to infer whether destabilization of the particles was occurring.

The absorption spectra were used to determine the stability of the NS, while the corresponding heat output was used to look at the effects of instability. Being one of the initial studies done, our NS synthesis procedure was still in development yielding NS with an absorption wavelength around 700 nm. The laser system used here was the 1064 nm system.

Shown below are the UV-vis-NIR spectra (Figure 3.7) and heat profiles (Figure 3.8) of the NS on 2 consecutive days. The blue curve is the spectra taken just after creation while the orange curve is the spectra taken after overnight storage. 40 μL of 5% Citrate solution was added to the sample immediately after it was made. The curve contains a slight blueshift indicating an alteration of the NS. We think this maybe because the arms of the AuNS shrink as time goes on. Our hypothesis is further confirmed by the fact that as the arms of the NS shrink, the UV-vis-NIR spectra also blueshifts to lower wavelengths, which resemble the spectra of the spherical seeds.

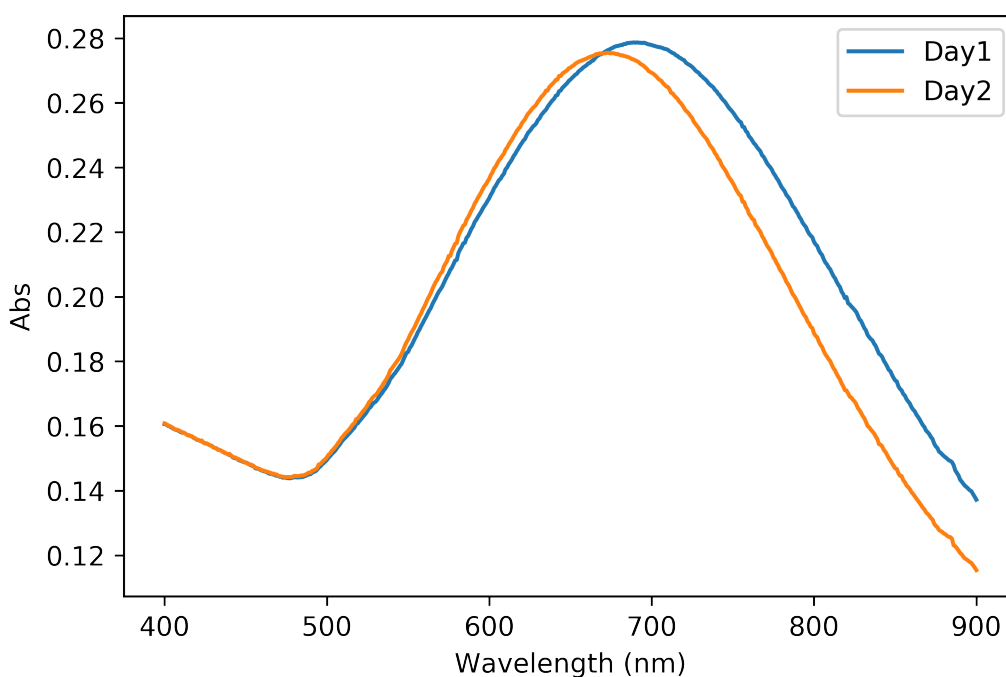


Figure 3.7: The figure shows the Vis-NIR-Spectra comparison of the AuNS on the first day of creation (Blue curve) and blueshift of the spectra on the second day (Orange curve)

We also see a considerable difference in the heat profiles of the NS on both days. Heating after overnight storage saw the heat output decrease by almost half the amount just after they were made (Figure 3.8). This indicated instability among the particles and prompted us to look at the NSs under a TEM.

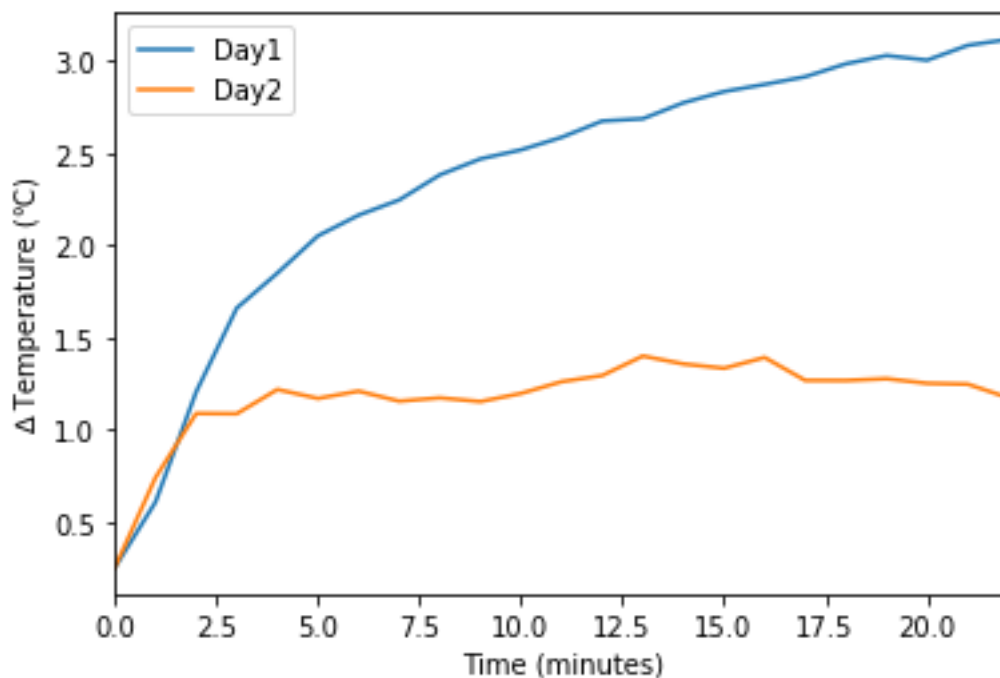


Figure 3.8: The graph alongside demonstrates the heating profile difference between the same sample heated on 2 consecutive days

Comparing the TEM images (Figure 3.9) of the samples from day 1, we don't see much of a difference between the images before and after exposure to the laser. However, we see a considerable decrease in NS arm lengths on Day2 after laser exposure as compared to before exposure. The NSs also appear to form clumps after heating on Day 2. This could be due to aggregation of NPs that has occurred after being exposed to the laser.

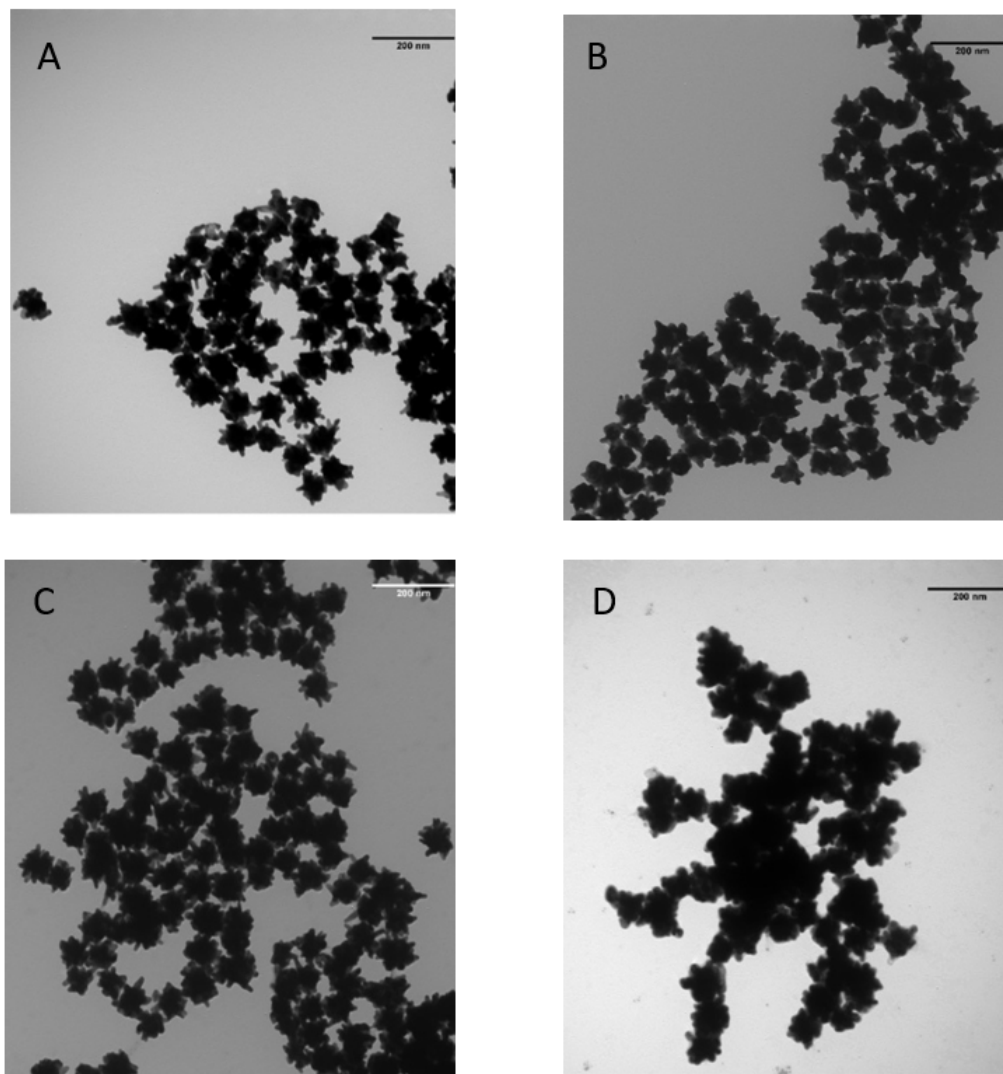


Figure 3.9: TEM Characterization of NS (A) Day1 before heating, (B) Day2 before heating, (C) Day1-After heating, (D) Day2-After heating

3.6.2 Effect of Citrate Buffer on stability of AuNS

After increasing the amount of seed and reducing the particles we were able to get the absorbance of the nanostars to be around 820 nm consistently. Knowing the NS undergo a blueshift, we attempted to stabilize them using a 5% citrate solution. 2 samples of AuNS (A and B) were used for this experiment and monitored for 7 days. The first sample (A) which is the NS solution without any citrate solution (Figure 3.10) and the second sample is B which is the NS solution with

the citrate solution (Figure 3.11). The citrate adds a negative surface charge to the surface of NS and prevents them from aggregating.[42]. Though citrate buffer reduced aggregation, there was a gradual blue shift of the NS spectrum over time. We think this blueshift occurs because the arms of the NSs reduce in length over the course of 7 days and become more spherical in shape. This change in shape causes the absorption spectra to blueshift as spherical NPs have a lower absorption wavelength. [43, 44, 45]

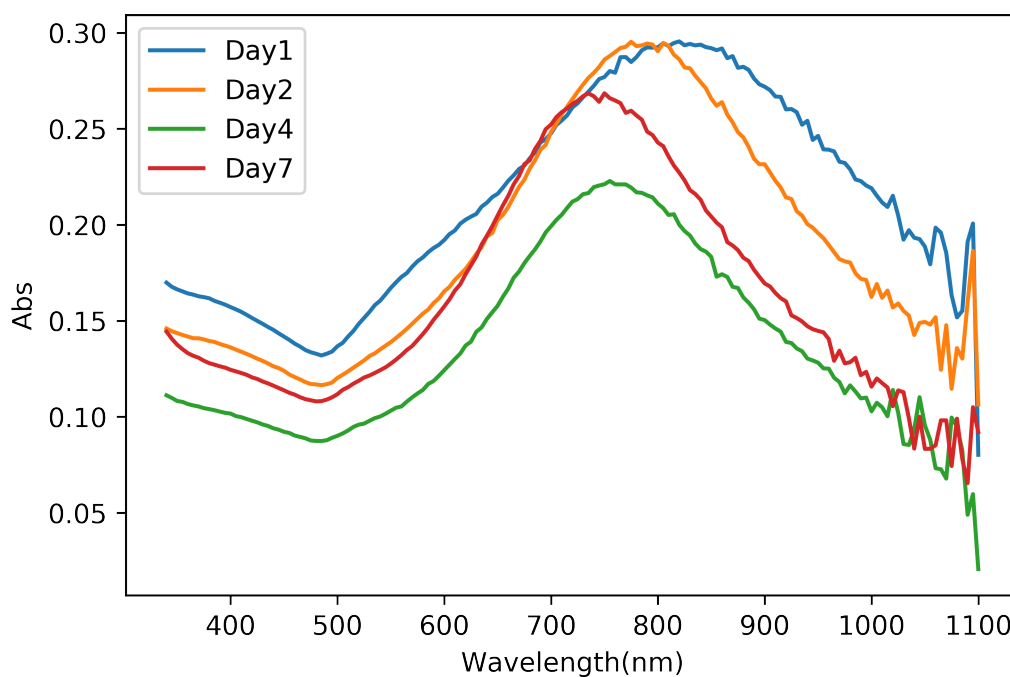


Figure 3.10: The graph demonstrates blueshift of NSs over a course of 1 week when they were not capped with a citrate buffer

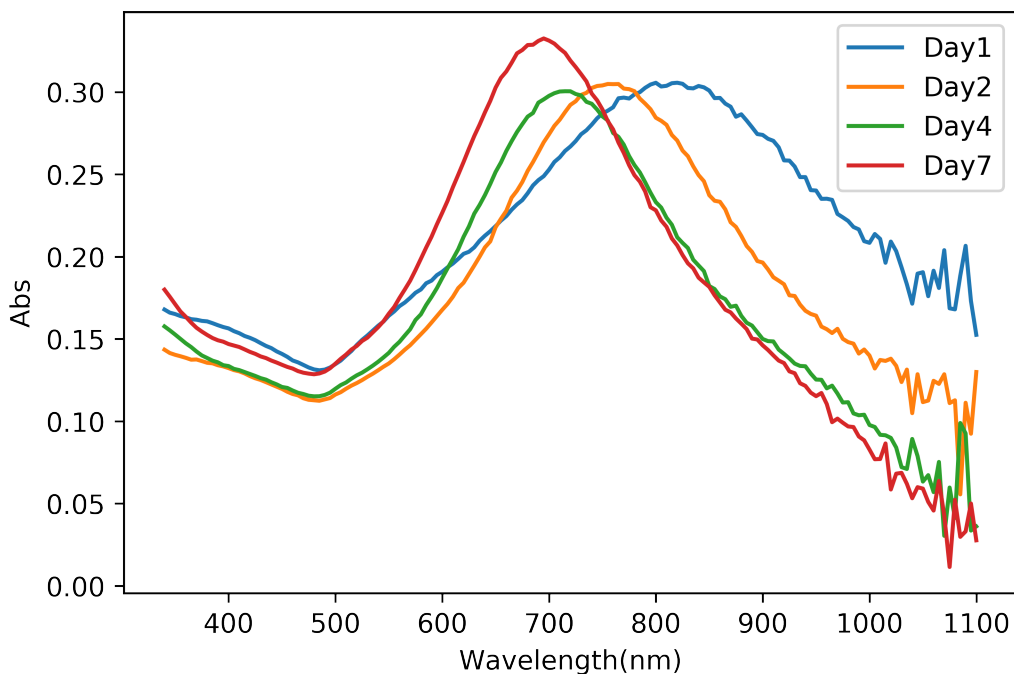


Figure 3.11: The graph demonstrates blueshift of NSs over a course of 1 week when they were capped with a citrate buffer

3.6.3 Effect of volume of sample

To determine the ideal volume of sample for heating experiments, the following experiment was performed on both 785 nm system and the 1064 nm system.

3.6.3.1 785 nm System

Figure 3.12 shows the heating data collected for the three volumes of AuNS samples. As expected, from the UV-vis-NIR data, we notice the 100 μL sample heated up the most with an average maximum increase of 8 $^{\circ}\text{C}$. We also notice a considerable drop in the heat outputs of the 200 μL and 300 μL samples averaging around 7 $^{\circ}\text{C}$. The heat output from both the sample volumes is similar and much lower than the 100 μL sample which could be caused by the cooling effects from the molecules around the area of dissipation. We also have a control sample of spherical NPs which heated up to 2 $^{\circ}\text{C}$.

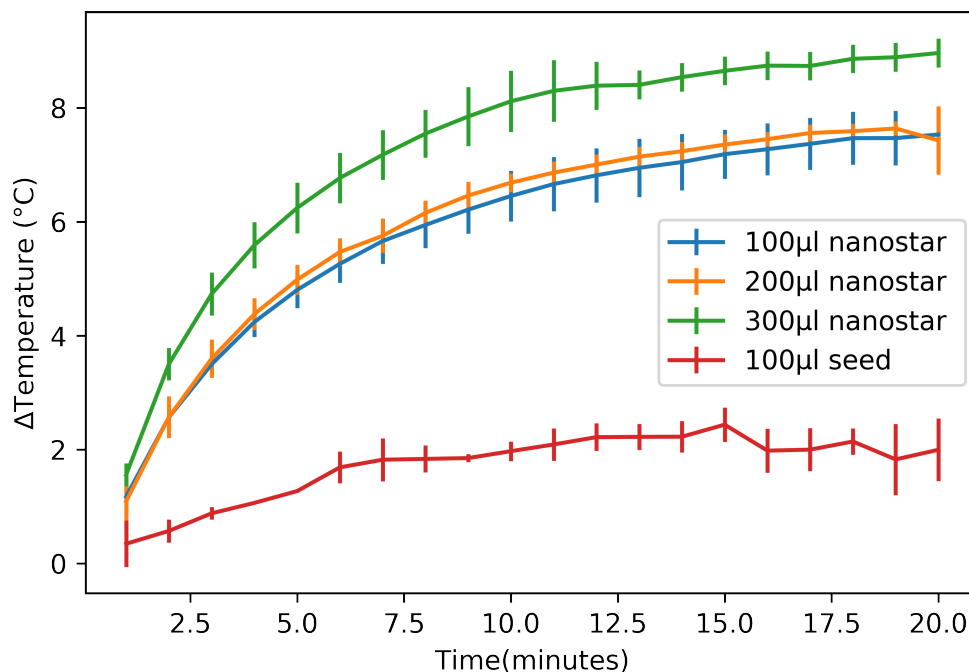


Figure 3.12: Heating data comparison of samples of AuNSs with differing volumes (300 μL , 200 μL and 100 μL) heated using the 785 nm laser system

3.6.3.2 1064 nm System

As described above, a similar procedure was implemented for the 1064 nm setup. AuNS were heated at full laser power of $165 \text{ mW}/\text{cm}^2$. A clear pattern was observed here with the 100 μL samples having an average heat output of $2.3 \text{ }^\circ\text{C}$. 200 μL samples had an average heat output of $2.1 \text{ }^\circ\text{C}$ and 300 μL samples had an average heat output of $1.36 \text{ }^\circ\text{C}$. We see closer resemblance of the 100 μL and 200 μL samples as compared to 300 μL and think this is mainly because of difficulty in securing the position of the thermocouple for different experiments because of system constraints. The 100 μL seed solution did not heat up in this system.

Unlike the 785 nm system, we see large decrease in heating in this system and think this is because of difficulty in maintaining controls with the system and the SPR of the NS frequency being further away from the 1064 nm laser frequency. (Figure 3.13)

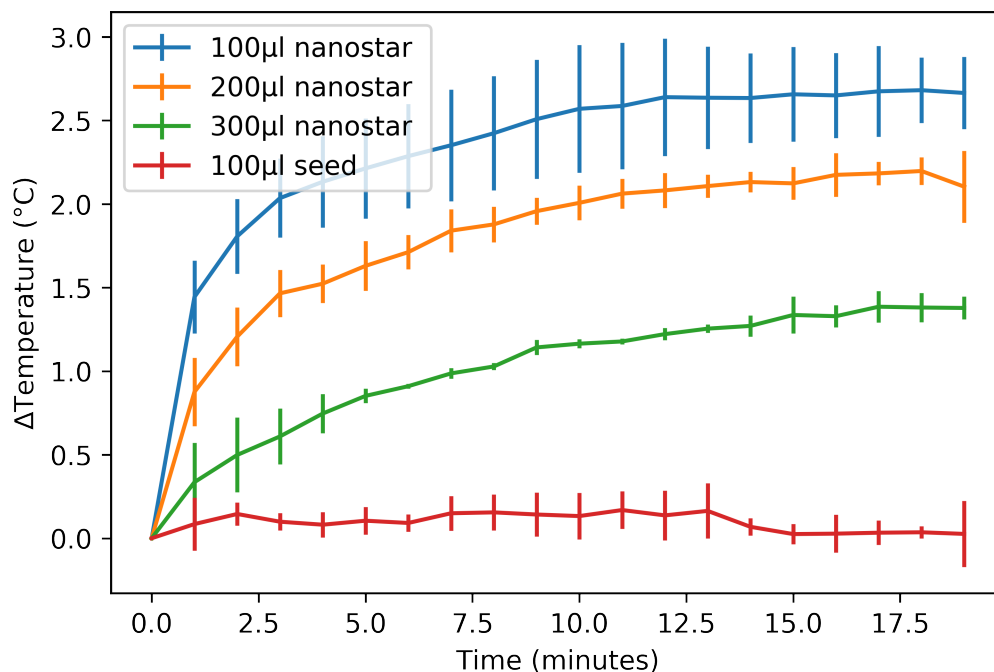


Figure 3.13: Heating data comparison of samples of AuNSs with differing volumes (300 μL , 200 μL and 100 μL) heated using the 1064 nm laser system

3.6.4 Change in morphology before and after heating

Our next experiment was performed to look at any induced effects the heating had on the NP. For this experiment, we compared the TEM and UV-vis-NIR data of the NS before and after heating. From the TEM data (Figure 3.14), we can visually infer there is no immediate observable difference in the length of the arms of the NS before and after irradiation with the laser. This result is further confirmed from the UV-vis-NIR data (Figure 3.15) wherein there is no blue shift in spectra before and after the sample has been exposed to heat. This indicated that the NPs have not reverted back to their more entropically favorable spherical form. We however notice a significant decrease in optical density of the NSs by 0.13 units before and after they have been exposed to the laser light. We also notice a broadening of the spectra peak which may indicate aggregation of the NSs due to the heat from the NPs.

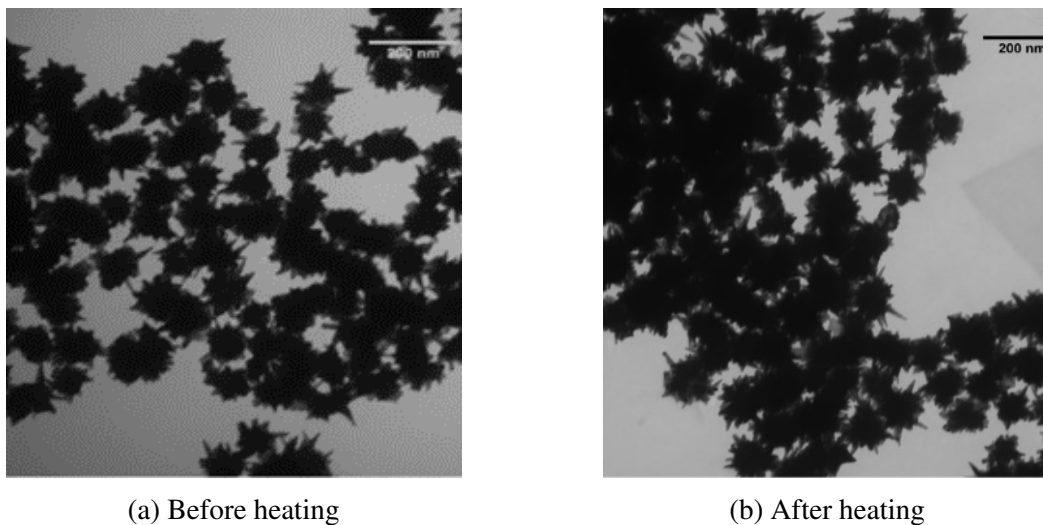


Figure 3.14: TEM image of NSs before and after being exposed to the laser light

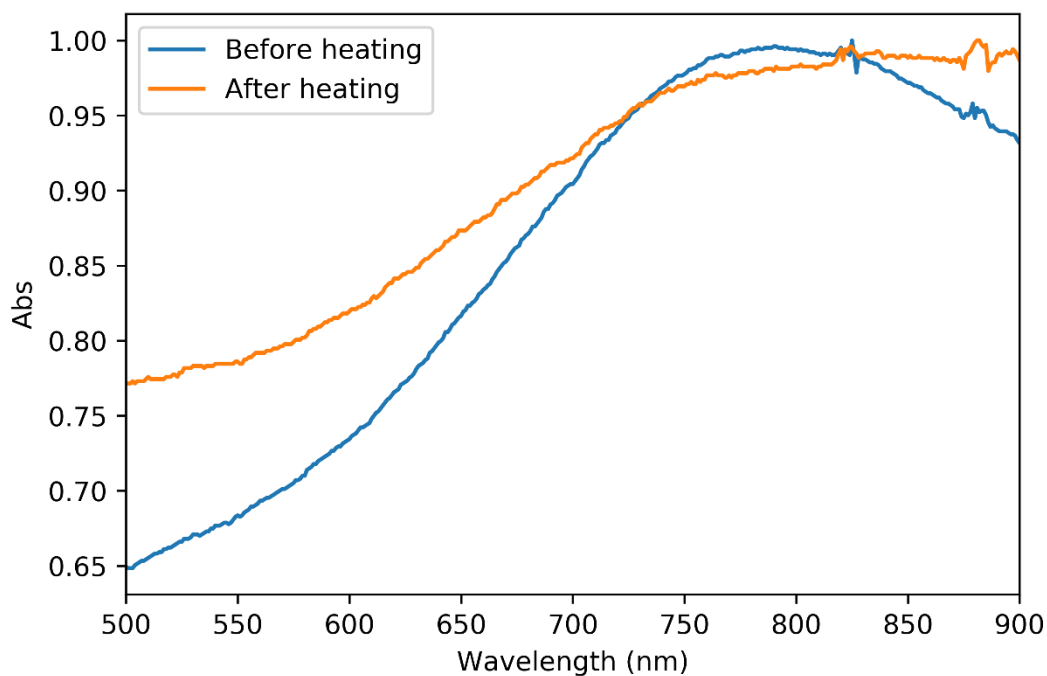


Figure 3.15: Normalized UV-vis-NIR Spectra of AuNS before and after being exposed to the NIR laser

3.6.5 Exposure to multiple heat and cool cycles

Our next experiment involved exposing the NS to multiple rounds of heating and cooling. Now aware that slight aggregation of the NS occurs due to the heat, we wanted to check the effects this may have on heating and cooling over a large duration. 20-minute heat and 15- minute cool cycles were chosen based on the temperature plateauing after exposure.

From the data, we notice a maximum heating of 6.8 °C for the first heat-cool cycle, 6.6 °C for the second heat-cool cycle and 6.4 °C for the heat-cool third cycle, ultimately the differences between the max temperatures (first and last) attributed to an approximate decrease of 6%. The slight decrease in heat output during every heat-cool cycle could be attributed to aggregation occurring due to the heat. (Figure 3.16)

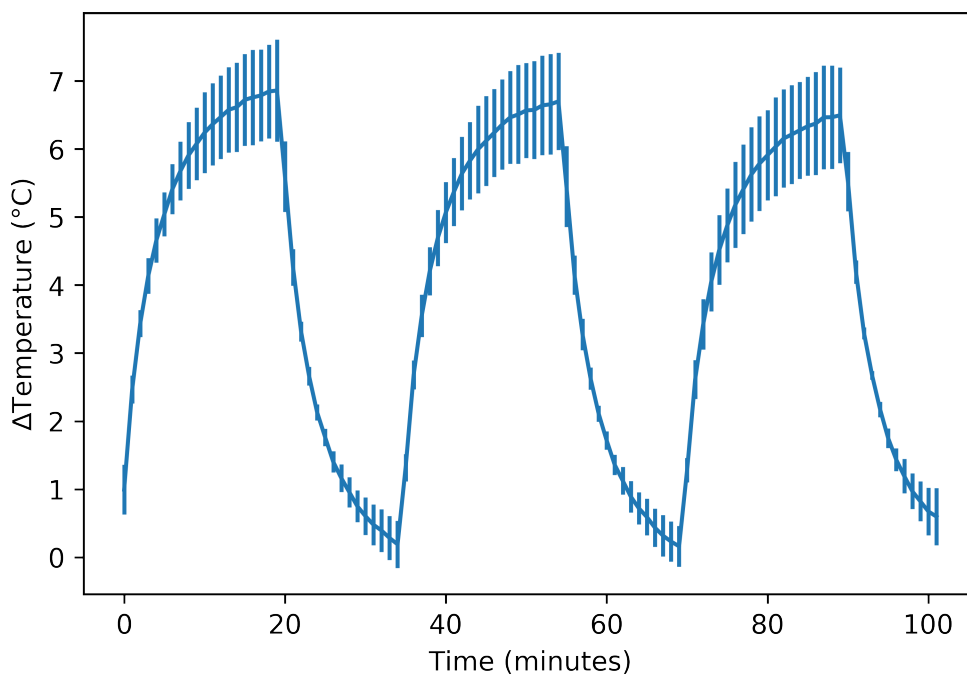


Figure 3.16: The figures demonstrate AuNS heated for 20-minute heat-15-minute cool cycles with the 785 nm laser system

3.7 AuNPr

3.7.1 Overnight storage of NPs and effects on shape and UV-vis-NIR spectra

As with the NS, we wanted to look at any changes that occurred to the NPr when stored overnight. The absorption spectra of the AuNPr is shown (Figure 3.17). The AuNPrs were stable after creation and did not need to be capped with any surfactant. The blue curve is the spectra taken just after the AuNPrs were created whereas the orange curve is the spectra of the NPrs taken after 24 h. Upon visible inspection, the spectra look identical and there isn't an observable change. This implies the NPrs are stable even after 24 h without the need of a capping or stabilizing agent unlike the NS which had a deviation in spectra even after capping with a stabilizing agent.

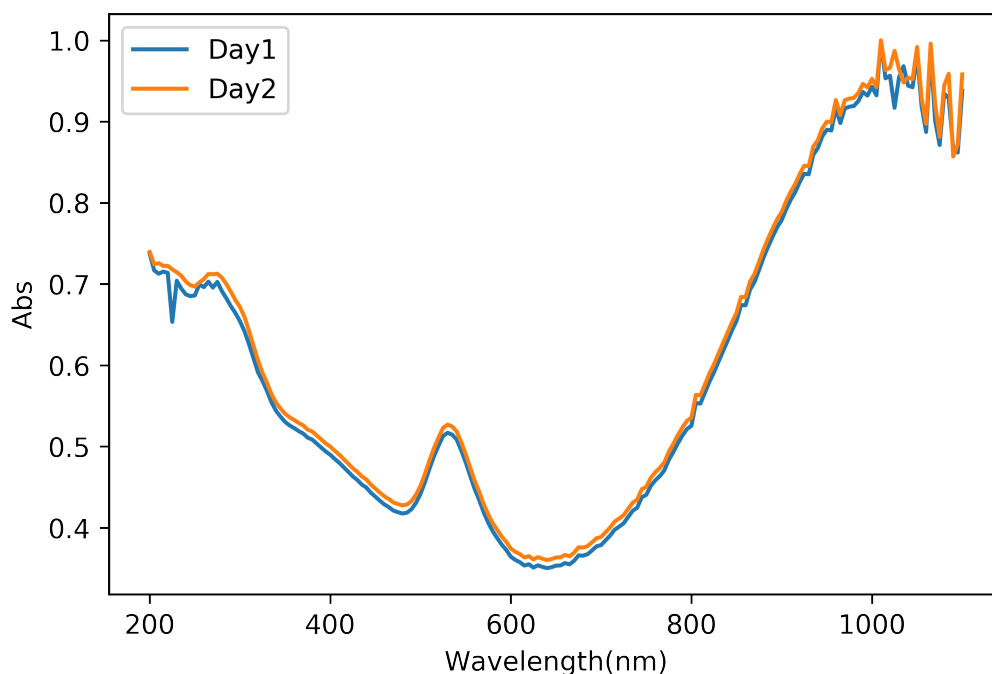


Figure 3.17: The figure shows the Absorption Spectra comparison of the AuNPr on the first day of creation (Blue curve) and the spectra on the second day (Orange curve)

We also see an identical heating profile of the NPrs when heated on both the days. Further confirming our assumption of that the NPrs were stable and had not deviated after storage. (Figure

3.18)

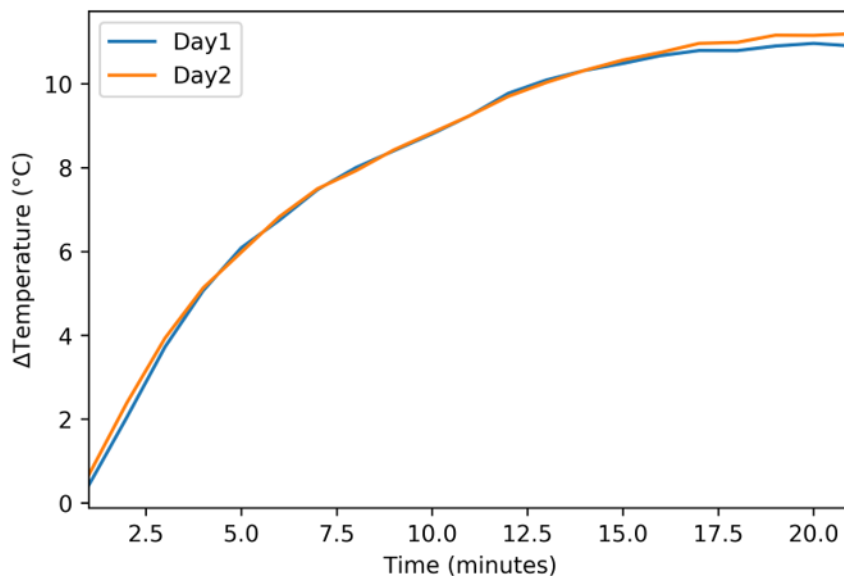


Figure 3.18: Heating profile of nanoprisms taken on 2 consecutive days after overnight storage at 4 °C

3.7.2 Effect of volume of sample

As with the NS, we wanted to look at the cooling effects when different volumes of NPrs were heated. Our experiment comprised of heating different volumes of AuNPr samples for 20 mins in both the systems. Volumes of 100 μL , 200 μL and 300 μL were used for the experiment.

3.7.2.1 785 nm System

AuNPrs exhibited a greater increase in heat output when compared to the NS in the same laser system, generating an average temperature just above 10°C for 100 μL sample, 9°C for 200 μL sample and 7°C for 300 μL sample. We see a clear decreasing trend between the samples which could be attributed to the cooling effects from surrounding molecules. (Figure 3.19)

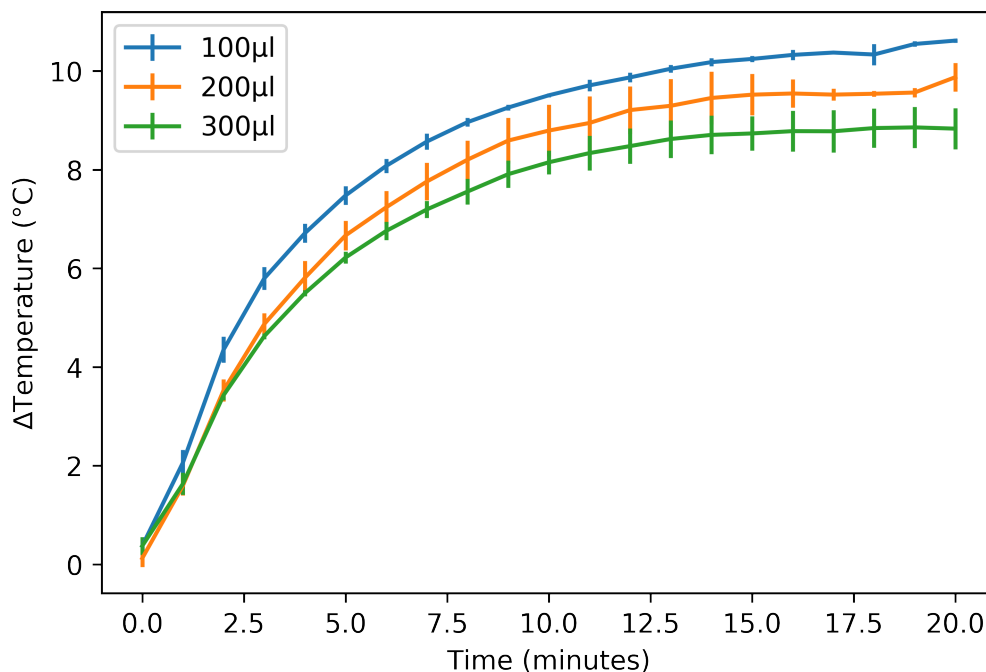


Figure 3.19: Heating data comparison of samples of AuNPrs with differing volumes (300 μL , 200 μL and 100 μL) heated using the 785 nm laser system

3.7.2.2 1064 nm system

As expected, AuNPrs exhibited a greater increase in heat output compared to the NS in the same system, generating an average temperature increase of 4 °C (Figure 3.20). Higher volumes of AuNPr also resulted in reduced heating as compared to lesser volumes of solution. 100 μL of AuNPr had an average heat output of 4°C whereas 200 μL had an average heat output of 3.56°C and 00 μL had an average of 1.68°C. We see large gaps in between the heat outputs for all 3 volumes. We think the decrease in heat output and gap in heat output between different volumes could be because of the lower power of the laser and inability to dissipate to larger areas and produce heating. This gap becomes more pronounced as the sample volumes increase. We observe barely any heating for the 300 μL sample.

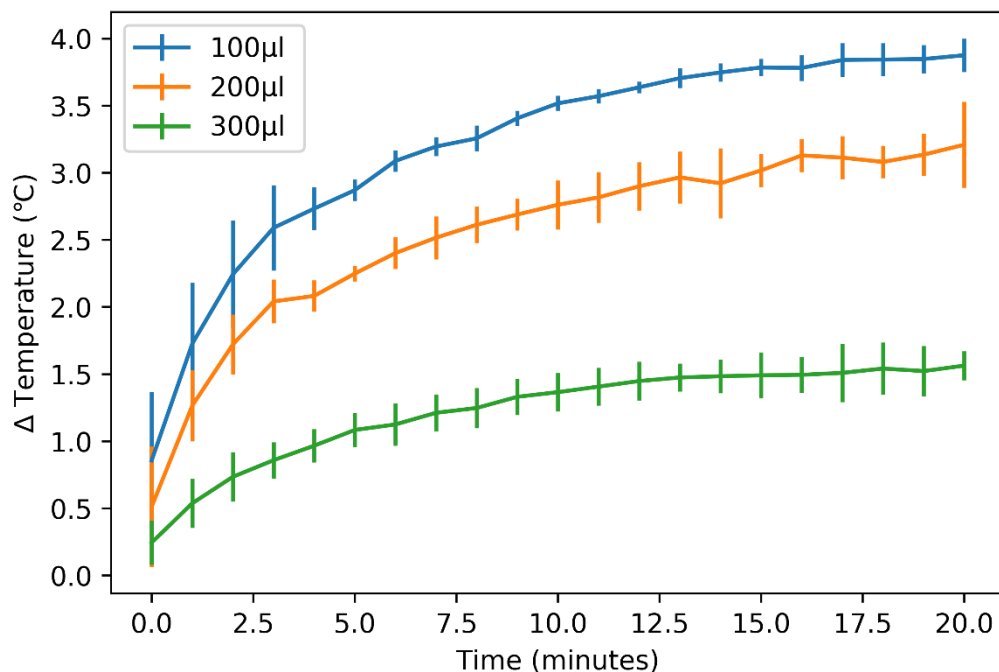


Figure 3.20: Heating data comparison of samples of AuNPr with differing volumes (300 μL , 200 μL and 100 μL) heated using the 1064 nm laser system

3.7.3 Change in morphology before and after heating

Like the NS, we wanted to see the effects the heating had on the NPRs morphology. From the TEM data (Figure 3.21), we observe large amounts of sticking between the NPRs after being exposed to the laser. We also see an increase in the scale of the second image in comparison with the first. Inferring from this, we think agglomeration has occurred due to the heat. From the UV-vis-NIR spectra (Figure 3.22), we observe an optical density difference of 0.08 units between the spectra before and after being exposed to the laser. We also notice a slight broadening of the spectra which could further indicate agglomeration of the particles after being exposed to the laser.

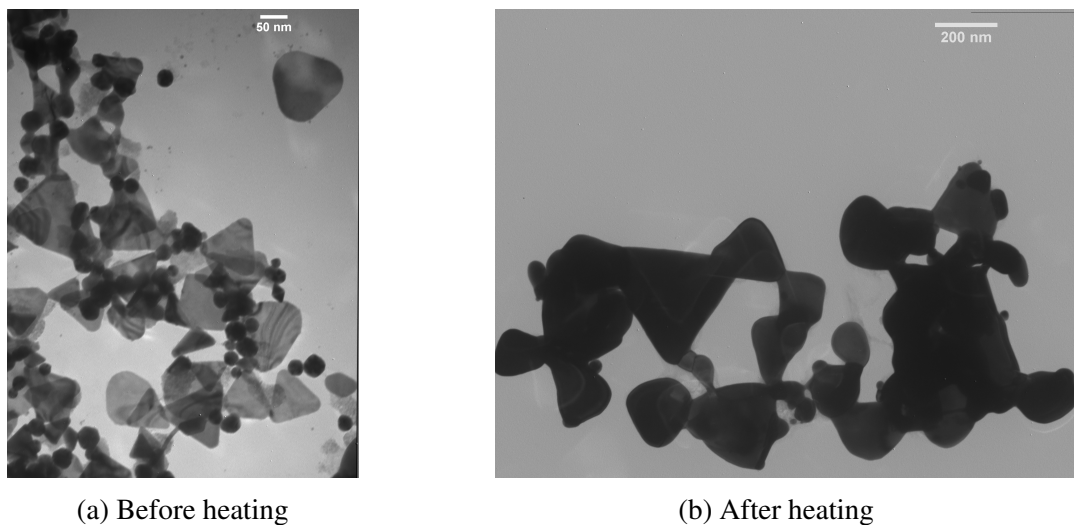


Figure 3.21: TEM image of NPr before and after being exposed to the laser light

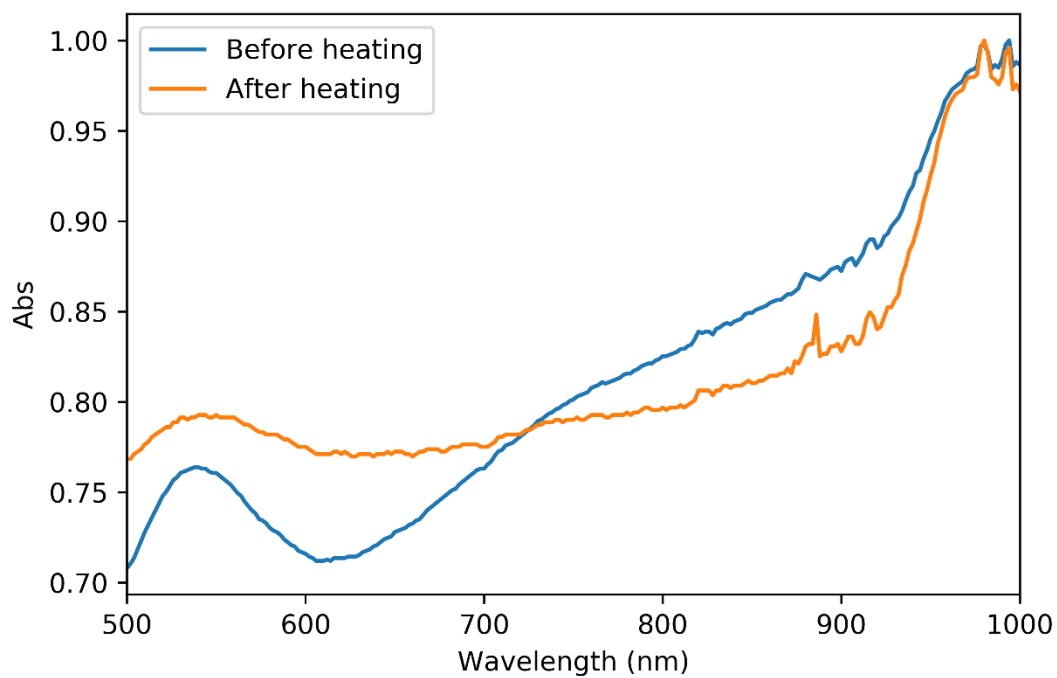


Figure 3.22: Normalized UV-vis-NIR Spectra of AuNPr before and after being exposed to the NIR Laser

3.7.4 Exposure to multiple heat and cool cycles

Like the NS, we wanted to look at the effects of multiple heat cool cycles on the NPRs for future pulsed applications. The heating data of NPR samples for 3 cycles of 20-min heat and 15-min cool are shown below. 20-minute heat and 15-minute cool cycles were chosen based on the temperature plateauing after exposure through a trial and error method. AuNPr appear to have much lesser variation between samples from the same batch when compared to the NS. We observe a maximum average heating of 11 °C among all 3 peaks and no decrease in heat output over the 3 cycles (Figure 3.23)

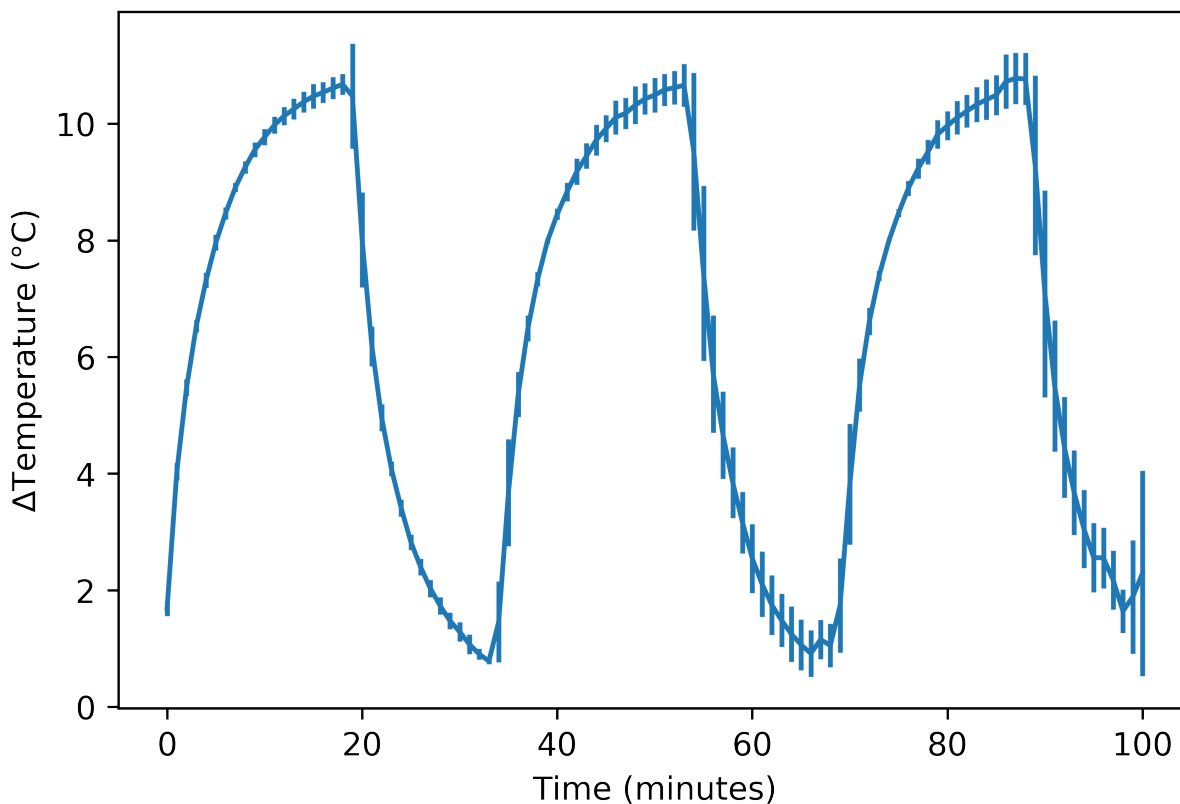


Figure 3.23: The figure demonstrates AuNPr heated for 20-minute heat-15-minute cool cycles with the 785 nm laser system

3.8 SERS Enhancement

SERS Enhancement was performed on the NPs for tracking the location inside the body. SERS Enhancement was performed using 2 different Raman reporters: MBA and BDT. For both we studied the Raman peaks at around 1081 cm^{-1} and 1591 cm^{-1} . [46, 47]

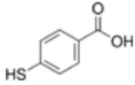
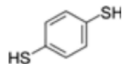
Molecule	Chemical Structure	Peak wavenumber (cm^{-1})	Peak Assignment
MBA		1089	v(C-S) stretch
		1589	v(C-C) ring stretch
BDT		1080	v(C-S) stretch
		1572	v(C-C) ring stretch

Table 3.1: Chemical structure and Peak assignments of 4-MBA and 1,4 BDT

3.8.1 MBA

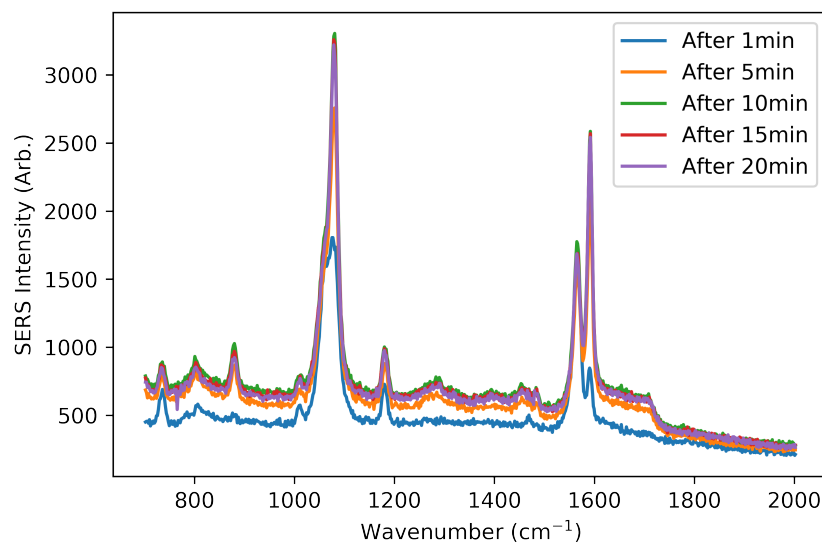


Figure 3.24: Complete SERS spectrum of MBA AuNS taken during a 20 min heating cycle

Figure 3.24 shows the complete SERS spectra observed for MBA absorbed onto the AuNS. The peaks observed at 1081 cm^{-1} and 1591 cm^{-1} corresponding to C-S and C-C ring vibrations were truncated and baseline corrected. Figures 3.25 and 3.26 show the differences in SERS signal for the two peaks observed during laser irradiation for 20 mins. There appears to be a decrease in SERS intensity for both the NS peaks during the 20-min heating cycle. The first peak has an initial absorbance just above 3500 and goes down to 2500 by the end of 20 mins while the second peak has an initial absorbance of 3000 and goes down to 2000 by the end of 20 mins.

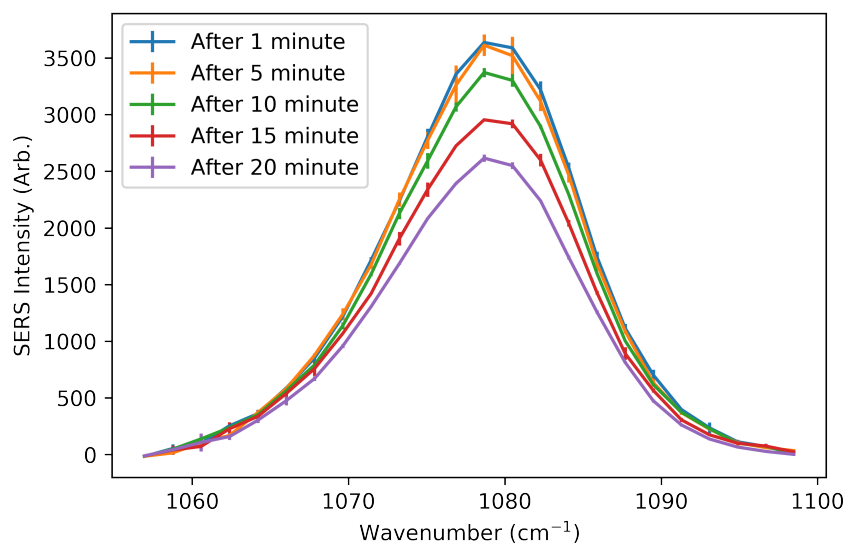


Figure 3.25: Comparison of SERS intensity change of MBA AuNS at 1081 cm^{-1} during 20-minute heating cycle

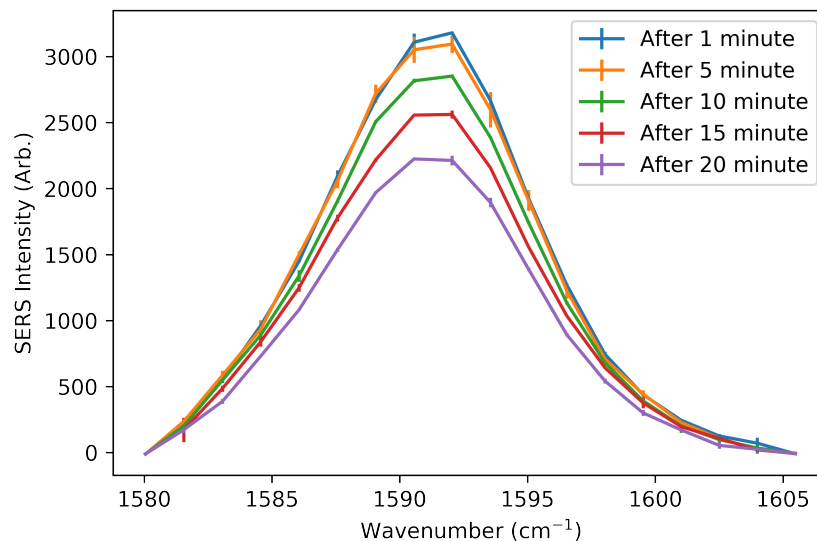


Figure 3.26: Comparison of SERS intensity change of MBA AuNS at 1591 cm^{-1} using 20-minute heating cycle

The plot of SERS intensity with respect to change in NS sample temperature is shown (figure 3.27). Peak 1 is the peak with Raman shift = 1081 cm^{-1} and peak 2 is a peak with Raman shift = 1591 cm^{-1} . As expected, for both the peaks, there is a decrease in SERS intensity as the temperature of the sample increases. The decrease in SERS intensity was seen to occur over 3 phases. The first phase saw a SERS decrease at the rate of 1 intensity value for every degree increase in temperature. This phase occurred during the first 5 minutes of heating. The second phase had a decrease rate of 80 intensity values for every degree increase in temperature. This phase occurred between the 5th and 12th minute of heating. The final phase saw a very large decrease rate of 700 intensity values for every degree increase in temperature which occurred from the 12th till the 20th minute. (Figure 3.27) This may be because the localized heat generated by the NS lead to the photodegradation of MBA that was attached to the NS thus causing a loss of SERS signal during heating.[48]

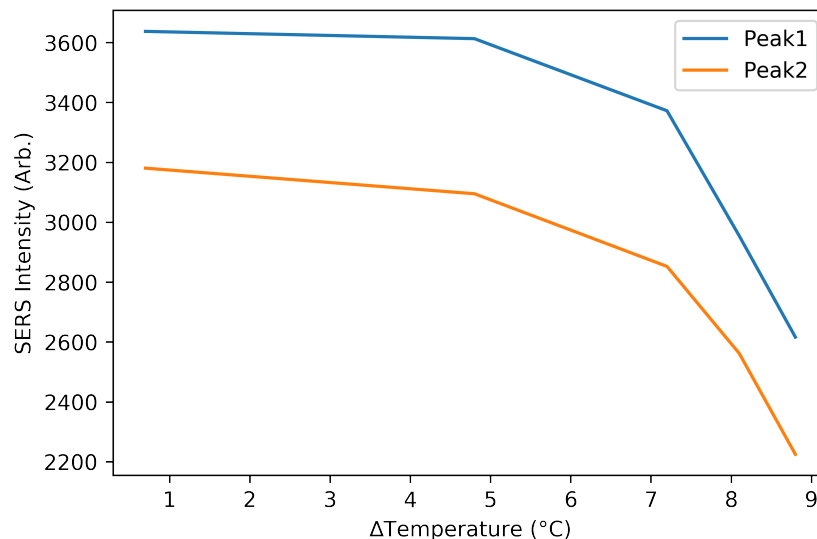


Figure 3.27: Comparison between SERS intensity change of MBA AuNS with temperature change of the sample during the 20-min heating cycle for peak1 (1081 cm^{-1}) and peak2 (1591 cm^{-1})

With the AuNPr, there is a different trend observed and the complete spectrum is shown in figure 3.28. Unlike the NS, we see an increase in SERS intensity for both the peaks (Figure 3.29 and 3.30) over the course of 20 mins. In the first 10 mins we see an initial large increase and then a more gradual increase for the remaining 10 mins of enhancement. Peak1 starts off at an absorbance of 400 and moves up to 1400 by the end of 20 mins whereas peak2 starts off with 100 and moves up to 800 by the end of 20 mins.

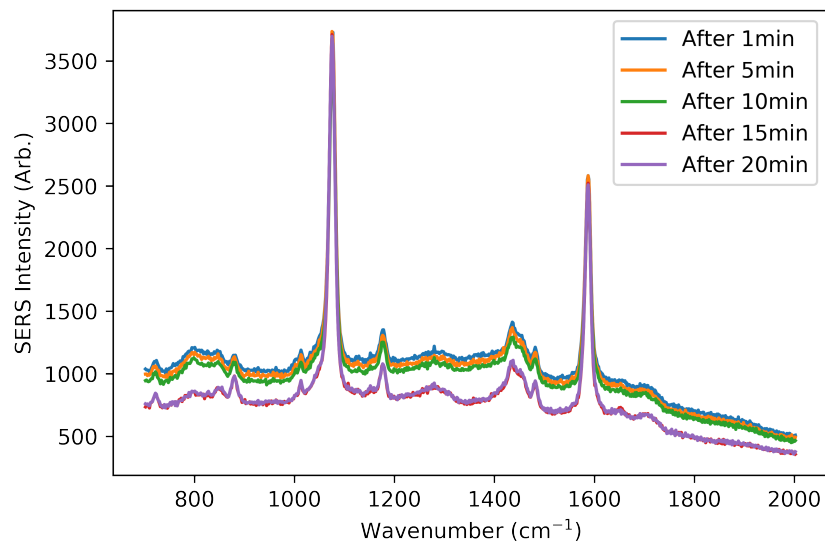


Figure 3.28: Complete SERS spectrum of MBA AuNPr taken during a 20 min heating cycle.

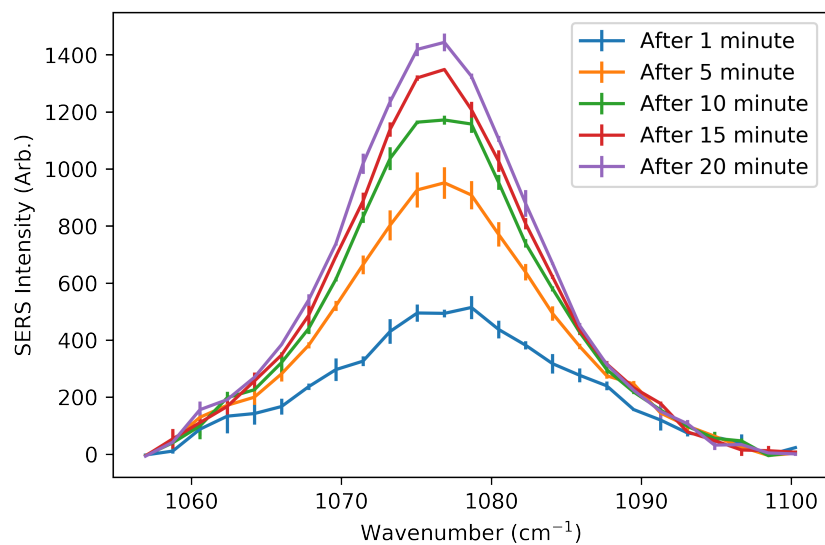


Figure 3.29: Comparison of SERS intensity change of MBA AuNPr at 1081 cm^{-1} during 20-minute heating cycle

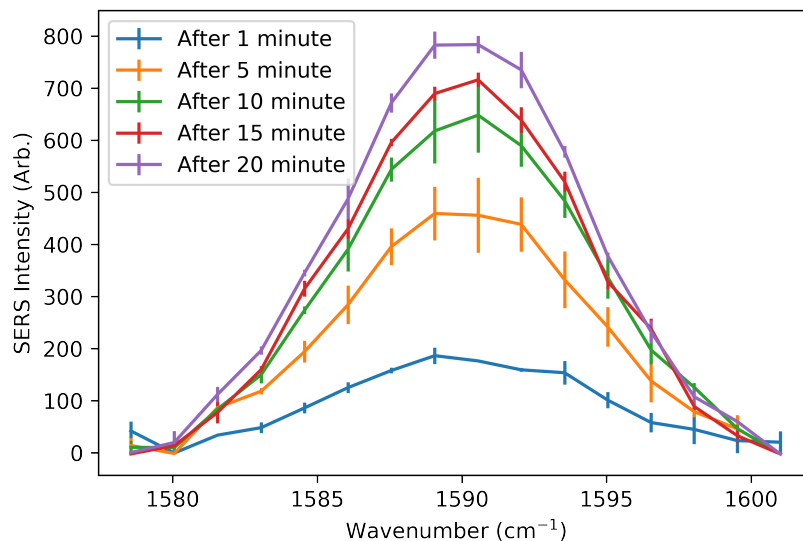


Figure 3.30: Comparison of SERS intensity change of MBA AuNPr at 1571 cm^{-1} during 20-minute heating cycle

The plot of Δ Temperature vs time shown below for the NPr (figure.3.31) wherein we see a gradual increase in SERS intensity over a temperature increase of 10 °C. Unlike the NS, we observe 1 main phase here with a slight increase at the very end of the heating. The phase has a SERS increase at the rate of 54 intensity values for every degree increase in temperature and this occurs during the first 10 mins. The next part sees a rapid increase in SERS intensity at the rate of 250 intensity values for every degree increase in temperature.(Figure 3.31)

The gradual increase in SERS intensity is most likely due to NPrs forming small aggregates. This causes a rapid increase in the number of hotspots formed. The size of these aggregates increases over time thus also increasing the number of hotspots that may be present. This causes an increase in the SERS Enhancement.[49] This theory is further confirmed as the NS don't form aggregates during heating, as proven during above experiments where there is also a decrease in SERS Enhancement.

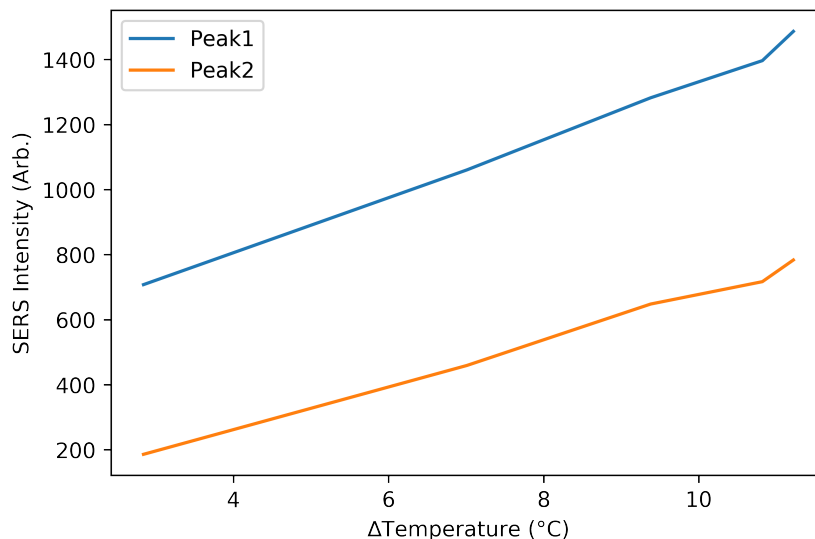


Figure 3.31: Comparison between SERS intensity change of MBA AuNPr with temperature change of the sample during the 20-minute heating cycle for peak1 (1081 cm^{-1}) and peak2 (1571 cm^{-1})

3.8.2 BDT

Shown is the SERS spectrum using the BDT Raman reporter for the AuNS (Figure 3.32). Both the BDT peaks (Figure 3.33 and 3.34) observed at 1081 cm^{-1} and 1591 cm^{-1} have been baseline corrected. There appears to be no increase or decrease in SERS enhancement for the NP enhanced with BDT. For the NS peak1, we see a slightly flat curve just below 1000 counts whereas the peak2 has an absorbance slightly above 1000 counts.

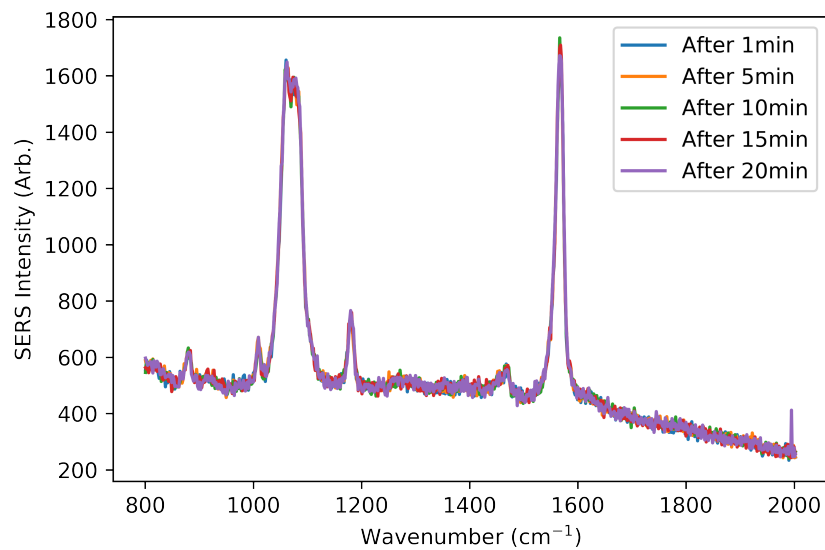


Figure 3.32: Complete SERS spectrum of BDT AuNS taken during a 20 min heating cycle.

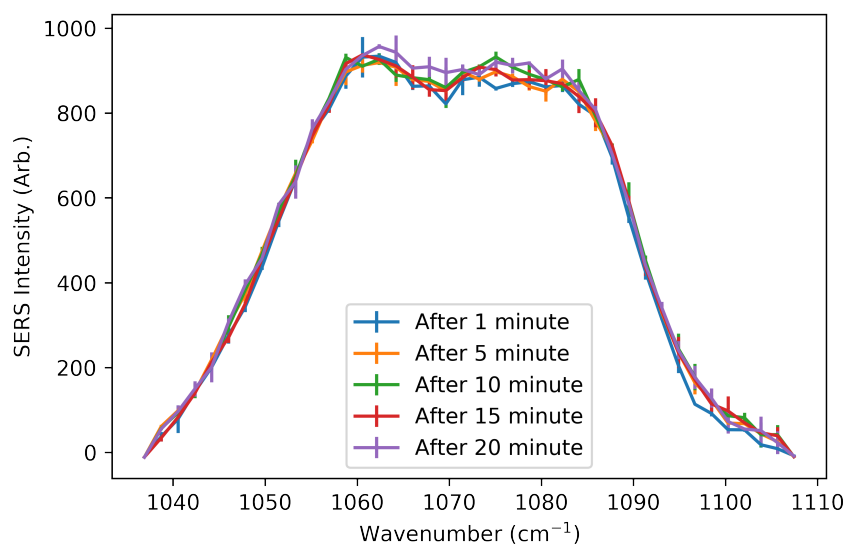


Figure 3.33: Comparison of SERS intensity change of BDT AuNS with a relatively flat enhancement during 20-minute heating cycle

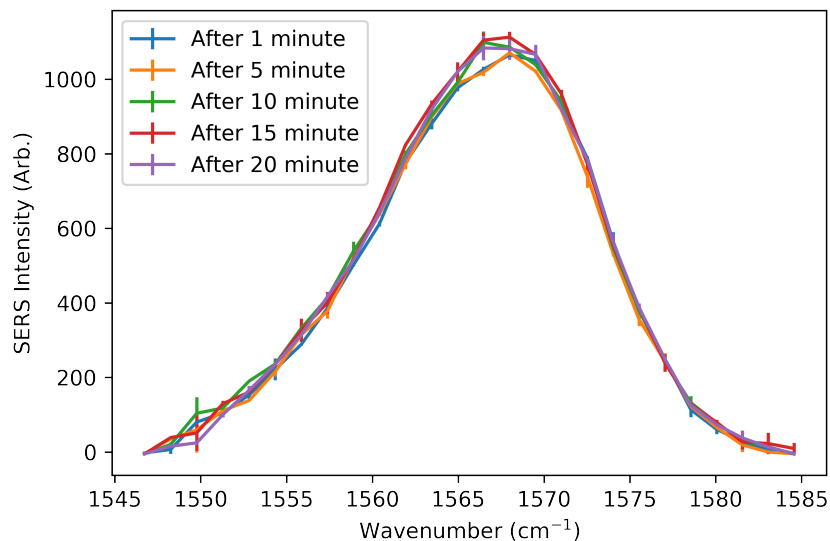


Figure 3.34: Comparison of SERS intensity change of BDT AuNS at 1571 cm^{-1} during 20-minute heating cycle

For the BDT NPRs, the SERS spectrum is shown in figure 3.35. Both the enhancement peaks have been individually baseline corrected and represented (Figure 3.36 and 3.37), we see a similar trend as seen with the BDT NS. Peak1 peaks at 1078 cm^{-1} with an absorbance of 600 intensity values. While Peak2 peaks at 1568 cm^{-1} with an absorbance intensity value of 600 as well. Unlike the MBA Raman reporter, we don't see any major increase or decrease in spectrum, we only see a very slight decrease in the spectrum for both peaks which lies in between the error bar brackets. We think this difference in spectra between MBA and BDT has occurred due to better binding of the MBA to the gold as compared to BDT Raman reporter[50] thus resulting in no change in the spectra.

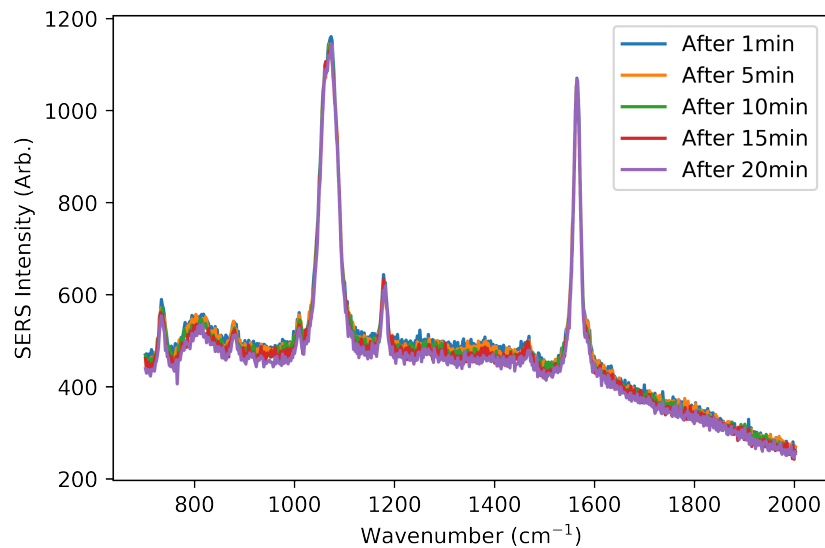


Figure 3.35: Complete SERS spectrum of BDT AuNPr taken during a 20 min heating cycle

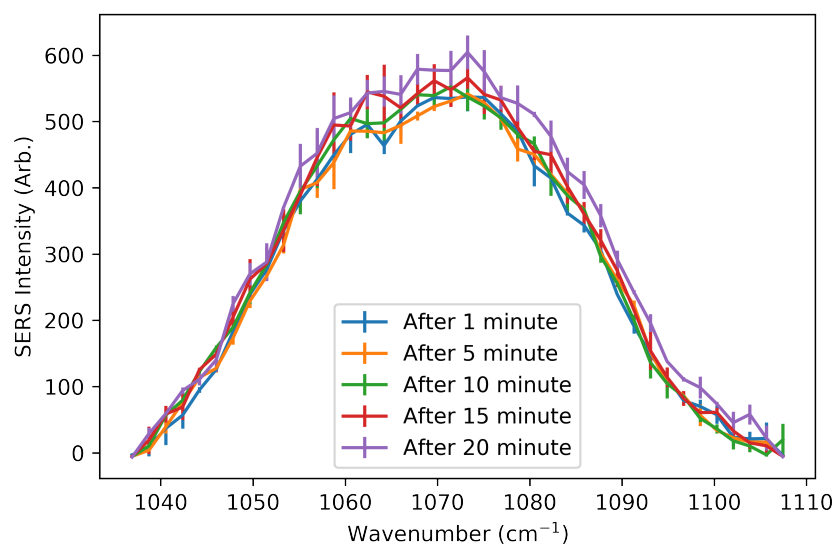


Figure 3.36: Comparison of SERS intensity change of BDT AuNPr with λ_{max} at 1078 cm^{-1} during 20-min heating cycle

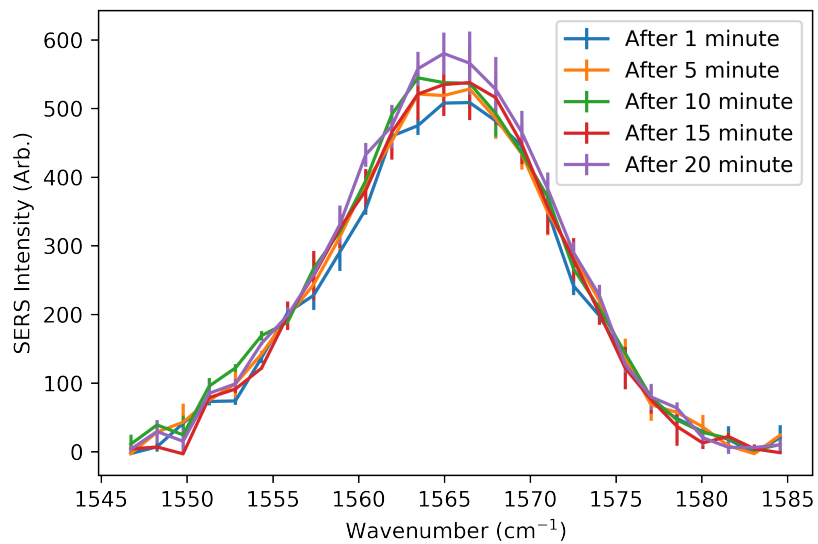


Figure 3.37: Comparison of SERS intensity change of BDT AuNPr with λ_{max} at 1571 cm^{-1} during 20-min heating cycle

4. SUMMARY AND CONCLUSIONS

In this thesis, we presented a novel method to enable easier measurement of heat output generated from irradiation of nanoparticles with a laser. The system went through various rounds of modifications and several iterations before it reached its present form. We started off with a 1064 nm laser system where we inserted the thermocouple into the cuvette from the top before every trial. We found this method to be very unreliable with huge variations between readings. We then shifted to a more compact system comprised of a 785 nm probe laser. We also updated the system design by inserting the thermocouple from a hole drilled on the side of the quartz cuvette. This system had exhibited minimal variations between temperature measurements and was easier to use.

This system for pre-screening nanoparticles to understand their heat generating capacity is more efficient than some of the other systems used by researchers in the field. By automating some of the parts it mimics a semi plug and play system where we insert the NPs into the cuvette, switch on the laser light and obtain the temperature measurements in MS-excel.

Using our system, we further explored the viability of using NS and NPrs for PTT. Based of literature, we started the heating experiments in the 1064 nm laser system with the NS. Unable to match the LSPR wavelengths of the NSs with the 1064 nm laser frequency, we explored NPrs which were known to have a LSPR frequencies well beyond 1000 nm. After ultimately shifting to the 785 nm system, we decided to pursue both NPs for our PT studies.

We tested different heating properties on both NSs and NPrs, such as the effect of sample volumes on heat output and the effect on heating when multiple cycles of heating and cooling were done on both the NS and NPrs. We then performed SERS enhancement on the NPs to look at tracking of the NPs with different Raman reporters. Both NPs excelled in different areas.

Efficient heating was observed using the NSs with an average heat increase of 7 °C. They also had a good SERS enhancement using MBA demonstrating the techniques potential use for tracking the NPs inside the body. However, the NS appeared to have a reduced absorption over the course of a few days after synthesis.

NPrs exhibited better heating than the NS and appeared stable over a period of 3 weeks without any change in morphology or absorption spectrum. However their synthesis method was not homogeneous and involved the formation of multiple spherical byproducts. They also appeared to form aggregates with the laser light exposure which also affected the SERS enhancement. In conclusion, we think NS are a much better PT agent compared to NPrs. They resemble the NPrs in heating but have morphology stability and do not aggregate when heated using the lasers. They also have a reliable SERS enhancement which can be used for tracking inside the body.

4.1 Future Work

Well aware from the above study that the NS have a good heat output, we plan to perform in vitro and ultimately in-vivo studies using the NS to test their effectiveness in destroying live tumor cells.

For our in-vitro application we plan to functionalize the NS with thiolated-polyethylene glycol (PEG) and incubate them with 3D tumor models developed by Dr. Adjei. The hypothesis is that particles of different morphologies and capping reagents will be able to populate different tissue domains within the tumor. Once accumulation of the particles has occurred we will be able to illuminate the site to modulate a photothermal response. Based on the data produced in this thesis, we believe that the heat output can be measured by co-functionalizing the particles with MBA and measuring the SERS response. Staining will be used to identify whether the cells surrounding the nanoparticle accumulation site are dead.

REFERENCES

- [1] R. Ellis, “Covid the third-leading cause of death in the u.s.,” 2020 (accessed August 18, 2020).
- [2] J. Vines, J.-H. Yoon, N.-E. Ryu, D.-J. Lim, and H. Park, “Gold nanoparticles for photothermal cancer therapy,” *Frontiers in Chemistry*, vol. 7, 04 2019.
- [3] C. E. Schmidt and J. B. Leach, “Neural tissue engineering: Strategies for repair and regeneration,” *Annual Review of Biomedical Engineering*, vol. 5, no. 1, pp. 293–347, 2003. PMID: 14527315.
- [4] P. Cherukuri and E. Glazer, “Targeted hyperthermia using metal nanoparticles,” *Advanced drug delivery reviews*, vol. 62, pp. 339–45, 11 2009.
- [5] R. Mout, D. F. Moyano, S. Rana, and V. M. Rotello, “Surface functionalization of nanoparticles for nanomedicine,” *Chem. Soc. Rev.*, vol. 41, pp. 2539–2544, 2012.
- [6] J. U. Menon, “Nanomaterials for photo-based diagnostic and therapeutic applications,” *Theranostics*, year = 2013, volume = 3, number = 1, pages = 152-166,.
- [7] H. Mendoza-Nava, G. Ferro-Flores, B. Ocampo-García, J. Serment-Guerrero, C. Santos-Cuevas, N. Jiménez-Mancilla, M. Luna-Gutiérrez, and M. A. Camacho-López, “Laser heating of gold nanospheres functionalized with octreotide: In vitro effect on hela cell viability,” *Photomedicine and Laser Surgery*, vol. 31, no. 1, pp. 17–22, 2013. PMID: 23140265.
- [8] J. H. Sakamoto, A. L. van de Ven, B. Godin, E. Blanco, R. E. Serda, A. Grattoni, A. Ziemys, A. Bouamrani, T. Hu, S. I. Ranganathan, E. De Rosa, J. O. Martinez, C. A. Smid, R. M. Buchanan, S.-Y. Lee, S. Srinivasan, M. Landry, A. Meyn, E. Tasciotti, X. Liu, P. Decuzzi, and M. Ferrari, “Enabling individualized therapy through nanotechnology,” *Pharmacological Research*, vol. 62, no. 2, pp. 57 – 89, 2010. Towards clinical applications of nanoscale medicines.

- [9] J. Yao, M. Yang, and Y. Duan, “Chemistry, biology, and medicine of fluorescent nanomaterials and related systems: new insights into biosensing, bioimaging, genomics, diagnostics, and therapy,” *Chemical reviews*, vol. 114, p. 6130—6178, June 2014.
- [10] T. A. Tabish, P. Dey, S. Mosca, M. Salimi, F. Palombo, P. Matousek, and N. Stone, “Smart gold nanostructures for light mediated cancer theranostics: Combining optical diagnostics with photothermal therapy,” *Advanced Science*, vol. 7, no. 15, p. 1903441, 2020.
- [11] X. Huang and M. A. El-Sayed, “Gold nanoparticles: Optical properties and implementations in cancer diagnosis and photothermal therapy,” *Journal of Advanced Research*, vol. 1, no. 1, pp. 13 – 28, 2010.
- [12] X. Huang, W. Qian, I. H. El-Sayed, and M. A. El-Sayed, “The potential use of the enhanced nonlinear properties of gold nanospheres in photothermal cancer therapy,” *Lasers in Surgery and Medicine*, vol. 39, no. 9, pp. 747–753, 2007.
- [13] J. Z. Zhang, “Biomedical applications of shape-controlled plasmonic nanostructures: A case study of hollow gold nanospheres for photothermal ablation therapy of cancer,” *The Journal of Physical Chemistry Letters*, vol. 1, no. 4, pp. 686–695, 2010.
- [14] Y.-F. Huang, K. Sefah, S. Bamrungsap, H.-T. Chang, and W. Tan, “Selective photothermal therapy for mixed cancer cells using aptamer-conjugated nanorods,” *Langmuir : the ACS journal of surfaces and colloids*, vol. 24, pp. 11860–5, 10 2008.
- [15] A. B. Bucharskaya, G. N. Maslyakova, N. I. Dikht, N. A. Navolokin, G. S. Terentyuk, A. N. Bashkatov, E. A. Genina, B. N. Khlebtsov, N. G. Khlebtsov, and V. V. Tuchin, “The plasmonic photothermal therapy of transplanted tumors in rats using gold nanorods,” pp. S2–46–S2–46, 2016.
- [16] S. Kim, Y.-S. Chen, G. Luke, M. Mehrmohammadi, J. Cook, and S. Emelianov, “Ultrasound and photoacoustic image-guided photothermal therapy using silica-coated gold nanorods: In-vivo study,” pp. 233 – 236, 11 2010.

- [17] H. S. Kim and D. Y. Lee, “Photothermal therapy with gold nanoparticles as an anticancer medication,” *Journal of Pharmaceutical Investigation*, vol. 47, pp. 19–26, 2016.
- [18] C. Murphy, T. Sau, A. Gole, C. Orendorff, J. Gao, L. Gou, S. Hunyadi Murph, and T. Li, “Anisotropic metal nanoparticles: Synthesis, assembly, and optical applications,” *The Journal of Physical Chemistry B*, vol. 109, pp. 13857–70, 08 2005.
- [19] B. R. Paoella, W. J. Gibson, L. M. Urbanski, J. A. Alberta, T. I. Zack, P. Bandopadhyay, C. A. Nichols, P. K. Agarwalla, M. S. Brown, R. Lamothe, Y. Yu, P. S. Choi, E. A. Obeng, D. Heckl, G. Wei, B. Wang, A. Tsherniak, F. Vazquez, B. A. Weir, D. E. Root, G. S. Cowley, S. J. Buhrlage, C. D. Stiles, B. L. Ebert, W. C. Hahn, R. Reed, and R. Beroukhim, “Copy-number and gene dependency analysis reveals partial copy loss of wild-type sf3b1 as a novel cancer vulnerability,” *eLife*, vol. 6, February 2017.
- [20] Wang, G. Liu, K. Leung, R. Loffroy, P.-X. Lu, and Y.-X. Wáng, “Opportunities and challenges of fluorescent carbon dots in translational optical imaging,” *Current pharmaceutical design*, vol. 21, 09 2015.
- [21] A. K. Abbas, Id, Y. Ethawi, G. Schmölder, S. Sherif, M. Narvey, and M. Seshia, “Review of biomedical applications of contactless imaging of neonates using infrared thermography and beyond,” 08 2018.
- [22] G. von Maltzahn, A. Centrone, J.-H. Park, R. Ramanathan, M. J. Sailor, T. A. Hatton, and S. N. Bhatia, “Sers-coded gold nanorods as a multifunctional platform for densely multiplexed near-infrared imaging and photothermal heating,” *Advanced Materials*, vol. 21, no. 31, pp. 3175–3180, 2009.
- [23] E. B. Dickerson, E. C. Dreaden, X. Huang, I. H. El-Sayed, H. Chu, S. Pushpanketh, J. F. McDonald, and M. A. El-Sayed, “Gold nanorod assisted near-infrared plasmonic photothermal therapy (pqtt) of squamous cell carcinoma in mice,” *Cancer Letters*, vol. 269, no. 1, pp. 57 – 66, 2008.

- [24] H. Zeng, M. Korbelik, D. I. McLean, C. MacAulay, and H. Lui, “Monitoring photoproduct formation and photobleaching by fluorescence spectroscopy has the potential to improve pdt dosimetry with a verteporfin-like photosensitizer,” *Photochemistry and Photobiology*, vol. 75, no. 4, pp. 398–405, 2002.
- [25] M. Rycenga, Z. Wang, E. Gordon, C. Cobley, A. Schwartz, C. Lo, and Y. Xia, “Probing the photothermal effect of gold-based nanocages with surface-enhanced raman scattering (sers),” *Angewandte Chemie International Edition*, vol. 48, no. 52, pp. 9924–9927, 2009.
- [26] H. Yuan, C. Khoury, H. Hwang, C. Wilson, G. Grant, and T. Vo-Dinh, “Gold nanostars: Surfactant-free synthesis, 3d modelling, and two-photon photoluminescence imaging,” *Nanotechnology*, vol. 23, p. 075102, 02 2012.
- [27] A. O. Govorov and H. H. Richardson, “Generating heat with metal nanoparticles,” *Nano Today*, vol. 2, no. 1, pp. 30 – 38, 2007.
- [28] G. Ramírez-García, M. Honorato Colin, E. De la Rosa, T. López-Luke, S. S. Panikar, J. d. Ibarra-Sánchez, and V. Piazza, “Theranostic nanocomplex of gold-decorated upconversion nanoparticles for optical imaging and temperature-controlled photothermal therapy,” *Journal of Photochemistry and Photobiology A: Chemistry*, vol. 384, p. 112053, 08 2019.
- [29] Y. Tian, W. Yi, L. Bai, P. Zhang, J. Si, X. Hou, Y. Deng, and J. Hou, “Lentian in-situ coated tungsten oxide nanorods as a nanotherapeutic agent for low power density photothermal cancer therapy,” *International journal of biological macromolecules*, vol. 137, p. 904–911, September 2019.
- [30] L. Au, D. Zheng, F. Zhou, Z.-Y. Li, X. Li, and Y. Xia, “A quantitative study on the photothermal effect of immuno gold nanocages targeted to breast cancer cells,” *ACS nano*, vol. 2, pp. 1645–52, 09 2008.
- [31] H. Yuan, C. Khoury, H. Hwang, C. Wilson, G. Grant, and T. Vo-Dinh, “Gold nanostars: Surfactant-free synthesis, 3d modelling, and two-photon photoluminescence imaging,” *Nanotechnology*, vol. 23, p. 075102, 02 2012.

- [32] B. Pelaz, V. Grazu, A. Ibarra, C. Magén, P. del Pino, and J. Fuente, “Tailoring the synthesis and heating ability of gold nanoprisms for bioapplications,” *Langmuir : the ACS journal of surfaces and colloids*, vol. 28, pp. 8965–70, 02 2012.
- [33] G. Alfranca Ramón, A. Artiga, G. Stepien, M. Moros, S. Mitchell, and J. Fuente, “Gold nanoprism-nanorod face off: Comparing the heating efficiency, cellular internalization and thermoablation capacity,” *Nanomedicine (London, England)*, vol. 11, 10 2016.
- [34] S. H. Gromkowski, J. Yagi, and C. A. Janeway Jr, “Elevated temperature regulates tumor necrosis factor-mediated immune killing,” *European Journal of Immunology*, vol. 19, no. 9, pp. 1709–1714, 1989.
- [35] I. Singh, R. Viscardi, I. Kalvakolanu, S. Calderwood, and J. Hasday, “Inhibition of tumor necrosis factor-alpha transcription in macrophages exposed to febrile range temperature. a possible role for heat shock factor-1 as a negative transcriptional regulator,” *The Journal of biological chemistry*, vol. 275, pp. 9841–8, 04 2000.
- [36] S. Cong, Y. Yuan, Z. Chen, J. Hou, M. Yang, Y. Su, Y. Zhang, L. Li, Q. Li, F. Geng, and Z. Zhao, “Noble metal-comparable sers enhancement from semiconducting metal oxides by making oxygen vacancies,” *Nature communications*, vol. 6, p. 7800, 07 2015.
- [37] W. Xie, L. Su, A. Shen, A. Materny, and J. Hu, “Application of surface-enhanced raman scattering in cell analysis,” *Journal of Raman Spectroscopy*, vol. 42, no. 6, pp. 1248–1254, 2011.
- [38] F. Fu, B. Yang, X. Hu, H. Tang, Y. Zhang, X. Xu, Y. Zhang, S. Touhid, X. Liu, Y. Zhu, J. Zhou, and J. Yao, “Biomimetic synthesis of 3d au-decorated chitosan nanocomposite for sensitive and reliable sers detection,” *Chemical Engineering Journal*, vol. 392, p. 123693, 12 2019.
- [39] Y.-X. Yuan, L. Ling, X. Wang, M. Wang, R. Gu, and L. Yao, “Surface enhanced raman spectroscopic readout on heavy metal ions based on surface self assembly,” *Journal of Raman Spectroscopy*, vol. 38, pp. 1280 – 1287, 10 2007.

- [40] X. Zhang, D. Han, Z. Pang, Y. Sun, Y. Wang, Y. Zhang, J. Yang, and L. Chen, "Charge transfer in an ordered Ag/Cu₂S/4-MBA system based on surface-enhanced Raman scattering," *The Journal of Physical Chemistry C*, vol. 122, 02 2018.
- [41] A. Kudelski, "Surface-enhanced Raman scattering study of monolayers formed from mixtures of 4-mercaptobenzoic acid and various aromatic mercapto-derivative bases," *Journal of Raman Spectroscopy*, vol. 40, pp. 2037 – 2043, 12 2009.
- [42] M. Morales, A. Bonifacio, V. Lughì, S. Marsi, S. Carrato, and V. Sergo, "Long-term stability of surfactant-free gold nanostars," *Journal of Nanoparticle Research*, vol. 16, 09 2014.
- [43] H. Richardson, M. Carlson, P. Tandler, P. Hernandez Martinez, and A. Govorov, "Experimental and theoretical studies of light-to-heat conversion and collective heating effects in metal nanoparticle solutions," *Nano letters*, vol. 9, pp. 1139–46, 02 2009.
- [44] D. Philip, "Rapid green synthesis of spherical gold nanoparticles using mangifera indica leaf," *Spectrochimica Acta Part A: Molecular and Biomolecular Spectroscopy*, vol. 77, no. 4, pp. 807 – 810, 2010.
- [45] S. Aryal, R. C. D. Nallasamy, N. Bhattarai, C. Kim, and H. Kim, "Spectroscopic identification of S-Au interaction in cysteine capped gold nanoparticles," *Spectrochimica Acta. Part A, Molecular and biomolecular spectroscopy*, vol. 63, pp. 160–3, 02 2006.
- [46] C. A. Szafranski, W. Tanner, P. E. Laibinis, and R. L. Garrell, "Surface-enhanced Raman spectroscopy of aromatic thiols and disulfides on gold electrodes," *Langmuir*, vol. 14, no. 13, pp. 3570–3579, 1998.
- [47] Horiba, "Raman data and analysis,"
- [48] C. Sun, M. Gao, and X. Zhang, "Surface-enhanced Raman scattering (SERS) imaging-guided real-time photothermal ablation of target cancer cells using polydopamine-encapsulated gold nanorods as multifunctional agents," *Analytical and bioanalytical chemistry*, vol. 409, 06 2017.

- [49] S. Jung, J. Nam, S. Hwang, J. Park, J. Hur, K. Im, N. Park, and S. Kim, “Theragnostic ph-sensitive gold nanoparticles for the selective surface enhanced raman scattering and photothermal cancer therapy,” *Analytical chemistry*, vol. 85, 07 2013.
- [50] Z. Sumeng, M. Hou, J. Li, L. Ma, and Z. Zhang, “Semi-quantitative analysis of multiple chemical mixtures in solution at trace level by surface-enhanced raman scattering,” *Scientific Reports*, vol. 7, 12 2017.

APPENDIX A

ARDUINO MICROCONTROLLER CODE

```
include "max6675.h"

int ktcSO = 8; int ktcCS = 9; int ktcCLK = 10; double a;

MAX6675 ktc(ktcCLK, ktcCS, ktcSO);

void setup() Serial.begin(9600); Serial.println("CLEARDATA"); //clears up any data left from
previous projects

Serial.println("LABEL,Time(sec),Temperature"); //always write LABEL, so excel knows the
next things will be the names of the columns (instead of Acolumn you could write Time for in-
stance)

Serial.println("RESETTIMER"); //resets timer to 0 // give the MAX a little time to settle de-
lay(500);

void loop() // basic readout test

Serial.print("Deg C = "); Serial.println(ktc.readCelsius()); //Serial.print("Deg F = "); //Se-
rial.println(ktc.readFahrenheit());

delay(500);

Serial.print("DATA,TIME,");

//Serial.print(","); //Serial.println(voltage);
```